Synchronized States of Power Grids and Oscillator Networks by Convex Optimization

Carsten Hartmann,[1,*] Philipp C. Böttcher,[1] David Gross,[2] and Dirk Witthaut[1,2,†]

[1] *Institute of Climate and Energy Systems, Energy Systems Engineering (ICE-1), Forschungszentrum Jülich, 52428 Jülich, Germany*

[2] *Institute for Theoretical Physics, University of Cologne, 50937 Cologne, Germany*

(Received 15 March 2024; revised 23 August 2024; accepted 20 September 2024; published 31 October 2024)

Synchronization is essential for the operation of ac power systems: all generators in the power grid must rotate with fixed relative phases to enable a steady flow of electric power. Understanding the conditions for and the limitations of synchronization is of utmost practical importance. In this article, we propose a novel approach to computing and analyzing the stable stationary states of a power grid or a network of Kuramoto oscillators in terms of a convex optimization problem. This approach allows us to systematically compute *all* stable states where the phase difference across an edge does not exceed $\pi/2$. Furthermore, the optimization formulation allows us to rigorously establish certain properties of synchronized states and to bound the error in the widely used linear power flow approximation.

DOI: 10.1103/PRXEnergy.3.043004

I. INTRODUCTION

A reliable supply of electricity is vital for our society. The operation of the electric power system relies on a stable, synchronized state of the grid: all generators operate at the same frequency close to the reference frequency of 50 or 60 Hz [1]. The strict phase locking enables a steady flow of electric power over long distances [2]. Violations of synchronization can occur after failures, disrupting power flows and eventually resulting in widespread power outages (see, e.g., Ref. [3]). Remarkably, similar problems occur in various systems studied in statistical physics. The Kuramoto model describes the dynamics of coupled limit-cycle oscillators [4–6] and bears strong similarities to models of coupled generators [7].

Because of their utmost importance, synchronization and stability are essential topics in various disciplines [8]. A central question is whether a given network supports a stable, fully synchronous state. Clearly, a strong coupling fosters synchronization, while a high power load impedes synchronization—but a comprehensive, rigorous answer to this question is still lacking. For general networks, accurate sufficient conditions were developed in Ref. [1] and sharpened in Ref. [9], while the role of the network topology was explored in Ref. [10]. For dense networks, a Lyapunov function was introduced in Ref. [11] that allows us to establish conditions for local and global stability. For an earlier review of direct methods based on Lyapunov theory, see Ref. [12]. A master stability function approach was introduced in Ref. [13], reducing the problem of synchronization stability to a simple spectral condition. Moreover, it has been realized that sparse networks can be multistable, i.e., they support more than one stable synchronized state [14]. Again, we are left with the question of when these states exist [15,16]. Another important question is how vulnerable a given synchronous state is to perturbations [17–19].

In this article, we propose an alternative approach to the synchronization problem in lossless networks by mapping the fixed-point equations to a convex optimization problem. In the case of potential multistability, each synchronous state is associated with an individual convex problem. This reformulation allows us to systematically compute all synchronized states or to refute their existence. Similar results were obtained by Jafarpour *et al.* [20], including an upper bound for the number of stable synchronized states. Here, we adopt a different perspective and thus provide further insights into the analytic and geometric properties of synchronized states. For instance, we provide an alternative view of the linear power flow or dc approximation widely used in power engineering [21]. The formulation as an optimization problem allows us to derive rigorous bounds on the error emerging from the linearization.

*Contact author: c.hartmann@fz-juelich.de

†Contact author: d.witthaut@fz-juelich.de

This article is organized as follows. We first review essential models for power grid synchronization as well as the Kuramoto model in Sec. II. The mathematical background and important prior results on the subject are summarized in Sec. III. The main result—the optimization approach—is formulated in Sec. IV. The relation to the linear or dc power flow equations is analyzed in Sec. V. Geometric aspects of the power flow optimization problem are discussed in Sec. VI. We close with a summary and an outlook for future research in Sec. VII.

II. STATIONARY STATES IN POWER GRIDS AND OSCILLATOR NETWORKS

In this section, we review models for the dynamics of electric power grids and coupled limit-cycle oscillators. In all cases, the stationary state is described by a set of nonlinear algebraic equations, which is the central objective of this article.

A. The swing equation and the classical model

Synchronous generators traditionally form the backbone of electric power generation. The state of the nth machine is characterized by the mechanical and electric phase angle $\theta_n(t)$, with a frame of reference rotating at the nominal frequency of the grid. The phase angle evolves according to the *swing equation* [12,21]

$$M_n\ddot{\theta}_n + D_n\dot{\theta}_n = p_n^{\mathrm{mech}} - p_n^{\mathrm{el}}, \tag{1}$$

where $p_n^{\mathrm{mech}}(t)$ is the mechanical input power provided to the generator, $p_n^{\mathrm{el}}(t)$ is the power delivered to the grid, M_n is an inertia constant, and D_n is a damping constant.

Furthermore, a model for the load nodes is needed to close the equations of motion [2]. One classical approach assumes load nodes to be fully passive and describes them as constant impedances to the ground. These nodes can be eliminated from the network equations, a process commonly referred to as "Kron reduction" [22,23]. The resulting model includes only generator nodes. If Ohmic losses are neglected, the electric power exchanged with the grid can be written as

$$p_n^{\mathrm{el}}(t) = \Delta p_n^{\mathrm{eff}} + \sum_m K_{nm}^{\mathrm{eff}} \sin(\theta_n(t) - \theta_m(t)),$$

with effective connectivity K_{nm}^{eff} and effective power injection $\Delta p_n^{\mathrm{eff}}$ accounting for the eliminated nodes. The stationary states of the grid are thus given by the nonlinear algebraic equations

$$p_n^{\mathrm{eff}} = \sum_m K_{nm}^{\mathrm{eff}} \sin(\theta_n - \theta_m) \text{ for all generator nodes } n, \tag{2}$$

with $p_n^{\mathrm{eff}} = p_n^{\mathrm{mech}} - \Delta p_n^{\mathrm{eff}}$. Notably, the coupling matrix K_{nm}^{eff} now describes an effective network, not the physical power transmission grid. This matrix is typically full, i.e., all entries are nonzero [22].

We note that the coupling function in Eq. (2) is strictly sinusoidal only if Ohmic losses are neglected. The presence of losses introduces phase lags such that the coupling function reads $\sin(\theta_n - \theta_m - \gamma_{nm})$ [23]. Numerical studies of the role of the impact of these phase lags were presented in Refs. [24,25]. Theoretical results on multistability were obtained in Refs. [26–28].

B. The structure-preserving model

A different approach that conserves the network structure was suggested by Bergen and Hill [29]. The starting point is the observation that the real power drawn from the grid by a load node n typically increases with the frequency. Linearizing around the nominal frequency, we can thus write the load as

$$p_n^{\mathrm{demand}} = p_n^{\mathrm{demand},0} + D_n\dot{\theta}_n. \tag{3}$$

For a consistent description, we need the power injected into the grid, which is simply given by $p_n^{\mathrm{el}} = -p_n^{\mathrm{demand}}$. Then we can write the evolution equation for *all* nodes as

$$M_n\ddot{\theta}_n + D_n\dot{\theta}_n = p_n^{\mathrm{in}} - p_n^{\mathrm{el}}, \tag{4}$$

with $M_n = 0$ and $p_n^{\mathrm{in}} = -p_n^{\mathrm{demand},0}$ for load nodes and $p_n^{\mathrm{in}} = +p_n^{\mathrm{mech}}$ for generator nodes. If Ohmic losses are neglected, the real power flow between two arbitrary nodes n and m is given by

$$p_{n\to m} = K_{nm}\sin(\theta_n - \theta_m). \tag{5}$$

Hence, the equations of motion read

$$M_n\ddot{\theta}_n + D_n\dot{\theta}_n = p_n^{\mathrm{in}} - \sum_m K_{nm}\sin(\theta_n - \theta_m), \tag{6}$$

and the stationary states are given by the nonlinear algebraic equations

$$p_n^{\mathrm{in}} = \sum_m K_{nm}\sin(\theta_n - \theta_m) \text{ for all nodes } n. \tag{7}$$

We emphasize that this model includes all nodes (buses) and all edges (branches) of the network. If Ohmic losses are neglected, the coupling constants K_{nm} are proportional to the inverse of the reactance X_{nm}^{-1} for a transmission line (n,m) and $K_{nm} = 0$ if no such line exists. Hence, the model conserves the structure of the actual power grid, which is sparse, and we may interpret K_{nm} as a weighted adjacency matrix.

C. The Kuramoto model

The Kuramoto model describes the dynamics of coupled limit-cycle oscillators with applications in various scientific disciplines [4–6]. The similarity to models of power grid synchronization was pointed out by Filatrella *et al.* [7].

In the Kuramoto model, the position of an oscillator n along the limit cycle is encoded in a phase variable $\theta_n(t)$ that evolves according to the equations of motion

$$\frac{d\theta_n}{dt} = \omega_n^{(0)} + \sum_{m=1}^{N} K_{nm} \sin(\theta_m - \theta_n),$$

where $\omega_n^{(0)}$ denotes the natural frequency of the oscillator n, $K_{nm} = K_{mn} \geq 0$ is a coupling constant, and N denotes the number of oscillators in the network. The Kuramoto-Sakaguchi model extends the original model to include a phase lag in the coupling function [30], similar to the effect of Ohmic losses in the classical or structure-preserving model.

Traditionally, research on the Kuramoto model has focused on large systems ($N \to \infty$) and the transition from incoherence (all oscillators rotate incoherently with $\dot{\theta}_n \approx \omega_n^{(0)}$) to partial synchronization (a subset of oscillators lock their frequencies $\dot{\theta}_n$). An excellent introduction to this direction of research is given in Ref. [31].

More recently, finite systems and their fixed points have received increased attention. The fixed points are determined by the set of equations

$$\omega_n^{(0)} = \sum_{m=1}^{N} K_{nm} \sin(\theta_n - \theta_m) \text{ for all } n \in \{1, \ldots, N\},$$

which is equivalent to Eqs. (2) and (7) if we identify $\omega_n^{(0)}$ with p_n. Two lines of mathematical research deserve to be mentioned: First, several authors have exploited the equivalence to flow networks [1,15,16,26,32]. Second, the fixed-point equation can be complexified to remove the sine [33,34].

D. Stability of fixed points

For all of the models described above, one can show that a stationary state is stable if and only if the Laplacian matrix $\boldsymbol{L}$ with elements

$$L_{nm} = \begin{cases} -K_{nm} \cos(\theta_n - \theta_m) & \text{for } n \neq m, \\ \sum_l K_{nl} \cos(\theta_n - \theta_l) & n = m \end{cases}$$

has only positive eigenvalues except for a trivial zero eigenvalue corresponding to the eigenvector $(1, 1, \ldots, 1)^\top$ [2,35]. A sufficient condition for stability is that

$$\cos(\theta_n - \theta_m) > 0 \tag{8}$$

for all edges (n, m) in the network. Stationary states that violate this condition are typically, but not always, unstable [35]. In the following, we focus on the stationary states that satisfy the condition in Eq. (8) for all edges and refer to them as "normal" states or solutions.

E. The linear power flow or dc approximation

In power transmission grids, the phase difference $\theta_n - \theta_m$ along a transmission line (n, m) is typically small. Hence, it is often appropriate to linearize the sine in the expression for the real power flow. The steady state of a lossless power grid is then determined by the linear set of equations

$$p_n = \sum_m K_{nm} (\theta_n - \theta_m). \tag{9}$$

This approximation is referred to as the "linear power flow approximation" or the "dc approximation" because the resulting equations are mathematically equivalent to Kirchhoff's equations for dc electric circuits. The validity of the linear power flow approximation was studied numerically in Refs. [36,37].

III. MATHEMATICAL BACKGROUND

In this section, we turn to the mathematical analysis of the equations

$$p_n = \sum_m K_{nm} \sin(\theta_n - \theta_m) \text{ for all nodes } n \tag{10}$$

that describe the stationary state of a power grid or a set of Kuramoto oscillators. These are referred to as the "real power flow equations" in the following to distinguish from linear power flow or the load-flow equations, which also include the reactive power [2]. We start with general aspects of (linear) flow networks before we move to the nonlinear real power flow.

A. Flow networks and algebraic graph theory

We introduce some useful notation and review some important results from the literature. Consider a network with N vertices or nodes and M transmission lines or edges. Nodes are labeled as $n = 1, \ldots, N$, and the node set is denoted as $\mathfrak{V}$. Throughout this article, we assume that the network is connected. Edges are labeled either by their endpoints (n, m) or consecutively as $e = 1, \ldots, M$, and the set of edges is denoted as $\mathfrak{E}$. To keep track of the direction of power flows, we fix an orientation for each edge. That is, if the line $e \equiv (n, m)$ is oriented from n to m, then a positive flow points from n to m and a negative flow points from m to n. To keep track of the structure of the topology of the grid and the orientation, we define the node-edge

incidence matrix $\boldsymbol{E} \in \mathbb{R}^{N\times M}$ with components [38]

$$E_{ne} = \begin{cases} 1 & \text{if line } e \text{ starts at node } n, \\ -1 & \text{if line } e \text{ ends at node } n, \\ 0 & \text{otherwise.} \end{cases} \tag{11}$$

The edges' transmission capacities $K_e = K_{nm}$ are summarized in a diagonal matrix $\boldsymbol{K} = \mathrm{diag}(K_1, \ldots, K_M)$.

A node n is characterized by the power injection p_n or its natural frequency. All power injections are summarized in the vector $\boldsymbol{p} = (p_1, \ldots, p_N)^\top$, where the superscript $\top$ denotes the transpose of a vector or matrix. As we are dealing with lossless power grids, we assume that $\sum_n p_n = 0$ from now on. Furthermore, we define the vector of nodal phase angles $\boldsymbol{\theta} = (\theta_1, \ldots, \theta_N)^\top$. The real power flow of an edge e is denoted as f_e, and all flows are summarized in the vector $\boldsymbol{f} = (f_1, \ldots, f_M)^\top$.

For lossless power grids, the real power flows have to satisfy the continuity equation or Kirchhoff's current law (KCL)

$$p_n = \sum_{m=1}^{N} f_{(n,m)} \text{ for all } n \in \{1, \ldots, N\}. \tag{12}$$

This set of equations can also be written in a vectorial form as

$$\boldsymbol{p} = \boldsymbol{E}\boldsymbol{f}\,. \tag{13}$$

The problem admits a straightforward solution if we impose the linear power flow or dc approximation. The flows now read

$$\begin{aligned} f_{(n,m)} &= K_{nm}(\theta_n - \theta_m), \\ \boldsymbol{f} &= \boldsymbol{K}\boldsymbol{E}^\top\boldsymbol{\theta}. \end{aligned}$$

Substituting the last equation into KCL, we obtain

$$\boldsymbol{p} = \boldsymbol{E}\boldsymbol{K}\boldsymbol{E}^\top\boldsymbol{\theta} = \boldsymbol{L}\boldsymbol{\theta}, \tag{14}$$

where we have introduced the Laplacian matrix $\boldsymbol{L} \in \mathbb{R}^{N\times N}$ with components [38]

$$L_{nm} = \begin{cases} \sum_{l=1}^{N} K_{nl} & \text{for } n = m, \\ -K_{nm} & \text{if } n \neq m \text{ and } n, m \text{ are adjacent,} \\ 0 & \text{otherwise.} \end{cases} \tag{15}$$

Equation (14) is linear and can thus be solved for θ in a straightforward way:

$$\begin{aligned} \boldsymbol{\theta} &= \boldsymbol{L}^+\boldsymbol{p}, \\ \boldsymbol{f} &= \boldsymbol{K}\boldsymbol{E}^\top\boldsymbol{L}^+\boldsymbol{p}, \end{aligned}$$

where the superscript $+$ denotes the Moore-Penrose pseudoinverse.

We note that the equations above still include a gauge freedom: if we shift all phases θ_n by a constant, then the power flows will not change. This is reflected in the fact that the Laplacian matrix of a connected network has rank $N - 1$. A typical choice in applications is to fix the phase of one distinguished slack node as $\theta_n \equiv 0$ and remove this node from the set of equations (14). Removing the respective row and column from $\boldsymbol{L}$, we obtain a *grounded* Laplacian matrix.

B. Cycle flows and Helmholtz decomposition

Before we proceed with the real power flow, we provide some further results on network flows. We recall that we assume that the network is connected throughout this article.

We first note that KCL (13) is underdetermined such that the general solution can be written as

$$\boldsymbol{f} = \boldsymbol{f}^{(0)} + \boldsymbol{f}^{(c)},$$

where $\boldsymbol{f}^{(0)}$ is a special solution and $\boldsymbol{f}^{(c)}$ denotes an arbitrary solution of the associated homogeneous equation, i.e., a vector from the kernel of the node-edge incidence matrix $\boldsymbol{E}$. The vectors $\boldsymbol{f}^{(c)}$ correspond to cycle flows: the power balance $\boldsymbol{E}\boldsymbol{f}^{(c)}$ vanishes everywhere, implying that no real power flows in or out of the network. We can fix a basis for the kernel by choosing $M - N + 1$ independent fundamental cycles and encode this basis in the edge-cycle incidence matrix $\boldsymbol{C} \in \mathbb{R}^{M\times(M-N+1)}$ with components

$$C_{e\beta} = \begin{cases} 1 & \text{if edge } e \text{ belongs to cycle } \beta, \\ -1 & \text{if the reverse edge } e \text{ belongs to cycle } \beta, \\ 0 & \text{otherwise,} \end{cases} \tag{16}$$

such that $\boldsymbol{E}\boldsymbol{C} = \boldsymbol{0}$. An important example is given by plane networks, i.e., networks that are drawn in the plane without any edge crossing. Here, one can choose the faces or plaquettes of the graph as fundamental cycles. After fixing a basis, we can write any cycle flow vector as

$$\boldsymbol{f}^{(c)} = \boldsymbol{C}\boldsymbol{\ell},$$

where $\boldsymbol{\ell} = (\ell_1, \ldots, \ell_{M-N+1})$ is a vector of cycle or loop flow amplitudes. We note that this decomposition proves to be useful in various linear power flow problems [39,40].

Similarly to the Helmholtz decomposition in vector analysis, a flow $\boldsymbol{f}$ can be decomposed into a cycle or source-free component $\boldsymbol{f}^{(c)} \in \ker(\boldsymbol{E})$ and a directed or irrotational component $\boldsymbol{f}^{(d)}$ as we make precise in the following lemma. We assume that the flow $\boldsymbol{f}$ is energy conserving, i.e., the sum of nodal outflows and inflows vanishes, $\sum_n (\boldsymbol{E}\boldsymbol{f})_n = 0$. A more detailed account of the topic can be found in Ref. [9].

Lemma 1. Any energy-conserving flow vector can be decomposed as

$$\boldsymbol{f} = \boldsymbol{f}^{(d)} + \boldsymbol{f}^{(c)}, \tag{17}$$

where $\boldsymbol{f}^{(c)} \in \ker(\boldsymbol{E})$ is a pure cycle flow and $\boldsymbol{f}^{(d)} \in \ker(\boldsymbol{C}^\top \boldsymbol{K}^{-1})$ by application of the projections

$$\begin{aligned} \boldsymbol{\Pi}_{\text{dir}} &= \boldsymbol{K}\boldsymbol{E}^\top \boldsymbol{L}^+ \boldsymbol{E}, \\ \boldsymbol{\Pi}_{\text{cycle}} &= \mathbb{1} - \boldsymbol{\Pi}_{\text{dir}}. \end{aligned} \tag{18}$$

The projectors are orthogonal with respect to the inner product

$$\langle \boldsymbol{\xi}, \boldsymbol{\zeta} \rangle_K := \sum_{e=1}^{M} \xi_e K_e^{-1} \zeta_e. \tag{19}$$

Proof. We first show that the two matrices are projections and span the entire space:

(1) The map $\boldsymbol{\Pi}_{\text{dir}}$ is a projection; that is,

$$\begin{aligned} \boldsymbol{\Pi}_{\text{dir}}^2 &= \boldsymbol{K}\boldsymbol{E}^\top \boldsymbol{L}^+ \underbrace{\boldsymbol{E}\boldsymbol{K}\boldsymbol{E}^\top}_{=\boldsymbol{L}} \boldsymbol{L}^+ \boldsymbol{E} \\ &= \boldsymbol{K}\boldsymbol{E}^\top \boldsymbol{L}^+ \boldsymbol{E} = \boldsymbol{\Pi}_{\text{dir}}. \end{aligned}$$

Here we use the fact that the Moore-Penrose pseudoinverse is a weak inverse in the sense that it satisfies $\boldsymbol{L}^+\boldsymbol{L}\boldsymbol{L}^+ = \boldsymbol{L}^+$.

(2) The map $\boldsymbol{\Pi}_{\text{cycle}}$ is a projection; that is,

$$\begin{aligned} \boldsymbol{\Pi}_{\text{cycle}}^2 &= (\mathbb{1} - \boldsymbol{\Pi}_{\text{dir}})^2 = \mathbb{1} - 2\boldsymbol{\Pi}_{\text{dir}} + \boldsymbol{\Pi}_{\text{dir}}^2 \\ &= \mathbb{1} - \boldsymbol{\Pi}_{\text{dir}} = \boldsymbol{\Pi}_{\text{cycle}}. \end{aligned}$$

(3) Finally, it is easy to see that

$$\boldsymbol{\Pi}_{\text{cycle}} + \boldsymbol{\Pi}_{\text{dir}} = \mathbb{1}.$$

Second, it is easy to see that the projections are orthogonal with respect to the inner product (19),

$$\langle \boldsymbol{\xi}, \boldsymbol{\Pi}_{\text{dir}} \boldsymbol{\zeta} \rangle_K = \boldsymbol{\xi}^\top \boldsymbol{E}^\top \boldsymbol{L}^+ \boldsymbol{E} \boldsymbol{\zeta} = \langle \boldsymbol{\Pi}_{\text{dir}} \boldsymbol{\xi}, \boldsymbol{\zeta} \rangle_K, \tag{20}$$

where we note that $\boldsymbol{E}^\top \boldsymbol{L}^+ \boldsymbol{E}$ is real symmetric.

Finally, we show that $\boldsymbol{\Pi}_{\text{cycle}}$ has the desired properties:

(1) For a pure cycle flow $\boldsymbol{f}^{(c)} \in \ker(\boldsymbol{E})$, we have

$$\boldsymbol{\Pi}_{\text{cycle}} \boldsymbol{f}^{(c)} = \boldsymbol{f}^{(c)}.$$

That is, the projector $\boldsymbol{\Pi}_{\text{cycle}}$ leaves any cycle flow invariant as desired.

(2) For an arbitrary flow vector $\boldsymbol{f}$, we have

$$\begin{aligned} \boldsymbol{E}\boldsymbol{\Pi}_{\text{cycle}}\boldsymbol{f} &= \boldsymbol{E}\left(\mathbb{1} - \boldsymbol{K}\boldsymbol{E}^\top \boldsymbol{L}^+ \boldsymbol{E}\right)\boldsymbol{f} \\ &= \boldsymbol{E}\boldsymbol{f} - \underbrace{\boldsymbol{E}\boldsymbol{K}\boldsymbol{E}^\top}_{=\boldsymbol{L}} \boldsymbol{L}^+ \boldsymbol{E}\boldsymbol{f}. \end{aligned}$$

Multiplying this by $\boldsymbol{L}^+$ from the left, we get

$$\begin{aligned} \boldsymbol{L}^+\boldsymbol{E}\boldsymbol{\Pi}_{\text{cycle}}\boldsymbol{f} &= \boldsymbol{L}^+\boldsymbol{E}\boldsymbol{f} - \boldsymbol{L}^+\boldsymbol{L}\boldsymbol{L}^+\boldsymbol{E}\boldsymbol{f} \\ &= \boldsymbol{L}^+(\boldsymbol{E}\boldsymbol{f} - \boldsymbol{E}\boldsymbol{f}) = \boldsymbol{L}^+\boldsymbol{0} = \boldsymbol{0}. \end{aligned}$$

Hence, we have found that $\boldsymbol{E}\boldsymbol{\Pi}_{\text{cycle}}\boldsymbol{f} \in \ker(\boldsymbol{L}^+)$. As we assume that the network is connected, the kernel of $\boldsymbol{L}^+$ is given by the linear subspace $\{c \cdot (1, \ldots, 1)^T | c \in \mathbb{R}\}$. We thus have

$$\boldsymbol{E}\boldsymbol{\Pi}_{\text{cycle}}\boldsymbol{f} = c \cdot (1, \ldots, 1)^T$$

for some c. On the other hand, by demanding that the flow is energy conserving, we have $\sum_n (\boldsymbol{E}\boldsymbol{\Pi}_{\text{cycle}}\boldsymbol{f})_n = 0$. This is fulfilled only if $c = 0$; that is,

$$\boldsymbol{E}\boldsymbol{\Pi}_{\text{cycle}}\boldsymbol{f} = 0.$$

We conclude that the projected flow $\boldsymbol{\Pi}_{\text{cycle}}\boldsymbol{f}$ is indeed a cycle flow as it is in the kernel of $\boldsymbol{E}$.

■

C. Resistance distance

A common metric in graph theory is the resistance distance or effective resistance [41]. It is defined via an analogy to dc electric circuits, with every edge a replaced with an Ohmic resistor. In this article, we assume that the conductance of an edge a is given by the coupling strength K_a, i.e., the resistance is K_a^{-1}. The resistance distance Ω_{nm} between two nodes n and m is then defined as the voltage drop between n and m divided by the total current between n and m. In the context of power grids, resistance distances provide essential information about the robustness of synchronized states [19].

To compute Ω_{nm}, we consider a unit current injected at node n and withdrawn at node m:

$$\boldsymbol{\iota}_{nm} = \boldsymbol{w}_n - \boldsymbol{w}_m,$$

where $\boldsymbol{w}_n$ is the nth standard basis vector; that is, $(\boldsymbol{w}_n)_l = \delta_{nl}$.

The nodal voltages are then given by the vector $\boldsymbol{u} = \boldsymbol{L}^{+}\boldsymbol{\iota}_{nm}$ such that we obtain

$$\begin{aligned}\Omega_{nm} &= \boldsymbol{\iota}_{nm}^{\top}\boldsymbol{u} \\ &= (\boldsymbol{w}_n - \boldsymbol{w}_m)^{\top}\boldsymbol{L}^{+}(\boldsymbol{w}_n - \boldsymbol{w}_m).\end{aligned}$$

If the nodes n and m are connected by an edge $a = (n, m)$, then we have $\boldsymbol{w}_n - \boldsymbol{w}_m = \boldsymbol{E}\boldsymbol{w}_a$ and thus

$$\Omega_a = \boldsymbol{w}_a^{\top}\boldsymbol{E}^{\top}\boldsymbol{L}^{+}\boldsymbol{E}\boldsymbol{w}_a. \tag{21}$$

Inserting $\mathbb{1} = \boldsymbol{K}^{-1}\boldsymbol{K}$, and recalling the definition of the projectors [Eq. (18)], we get

$$\begin{aligned}\Omega_a &= \boldsymbol{w}_a^{\top}\boldsymbol{K}^{-1}(\mathbb{1} - \boldsymbol{\Pi}_{\text{cycle}})\boldsymbol{w}_a \\ &= K_a^{-1}\left(1 - (\boldsymbol{\Pi}_{\text{cycle}})_{aa}\right).\end{aligned}$$

We note that the quantity $0 \leq (\boldsymbol{\Pi}_{\text{cycle}})_{aa} \leq 1$ is intimately connected to the connectivity of the endpoint of the edge a; it vanishes if the edge a is a bridge. Rigorous bounds for the quantity $1 - (\boldsymbol{\Pi}_{\text{cycle}})_{aa}$ in terms of the network topology were derived in Propositions 1 and 2 in Ref. [42].

D. Algebraic formulation and multistability of the real power flow equations

We now turn back to the real power flow equation (10). This problem is harder to tackle than the linear power flow due to the nonlinearity introduced by the sine function. In particular, the flows are now given by

$$\begin{aligned}f_{(n,m)} &= K_{nm}\sin(\theta_n - \theta_m), \\ \boldsymbol{f} &= \boldsymbol{K}\sin\left(\boldsymbol{E}^{\top}\boldsymbol{\theta}\right),\end{aligned} \tag{22}$$

where the sine function is taken elementwise. In general, the equations admit multiple solutions such that it is *a priori* unclear how and to which solution a numerical solver will converge. To systematically compute all solutions, one can proceed in two steps [16]. First, we compute all solution candidates; that is, all solutions of KCL (13). As described before, the general solution can be written as

$$\boldsymbol{f} = \boldsymbol{f}^{(0)} + \boldsymbol{f}^{(c)},$$

where $\boldsymbol{f}^{(c)}$ is an arbitrary cycle flow.

Now that we have a set of solution candidates, we have to select the actual solutions of the real power equations (10) from this set. Consider an edge $e \equiv (m, n)$. Inverting Eq. (22), we can recover the difference of the nodal phase angles at nodes m and n by

$$\begin{aligned}\theta_n - \theta_m &= \arcsin\left(\frac{f_e}{K_e}\right) \quad \text{or} \\ \theta_n - \theta_m &= \pi - \arcsin\left(\frac{f_e}{K_e}\right)\end{aligned} \tag{23}$$

modulo 2π. The first option leads to normal fixed points of Eq. (10) that are guaranteed to be stable. The second option typically (but not always) yields unstable solutions; hence, they will be discarded from now on. Insertion of the cycle flow decomposition $\boldsymbol{f} = \boldsymbol{f}^{(0)} + \boldsymbol{C}\boldsymbol{\ell}$ then yields

$$\theta_n - \theta_m = \arcsin\left(\frac{f_e^{(0)} + \sum_{\beta=1}^{M-N+1} C_{e\beta}\ell_\beta}{K_e}\right).$$

Trying to compute all phase angles typically results in a problem, as we cannot satisfy this relation simultaneously for all edges in the grid. Only for discrete values of the loop flow amplitudes $\boldsymbol{\ell}$ do we get a consistent solution. It has been shown that this is the case if the condition

$$\sum_{e=1}^{M} C_{e\alpha}\arcsin\left(\frac{f_e^{(0)} + \sum_{\beta=1}^{M-N+1} C_{e\beta}\ell_\beta}{K_e}\right) = 2\pi z_\alpha \tag{24}$$

with $z_\alpha \in \mathbb{Z}$ is satisfied for all fundamental cycles $\alpha = 1, \ldots, M - N + 1$ [16,32]. The interpretation of this condition is straightforward: If we add up all the differences $\theta_n - \theta_m$ around a cycle, the sum must equal zero or an integer multiple of 2π. Notably, if this condition is satisfied for the fundamental cycles, it is satisfied for all cycles.

The quantities z_α are referred to as "winding numbers," and we summarize them in the winding vector $\boldsymbol{z} = (z_1, \ldots, z_{M-N+1})^{\top}$. These winding numbers are particularly useful to characterize the solutions of the real power flow equations as they are unique (see Theorem 4.1 in Ref. [20]); that is, each normal solution corresponds to one unique value of the winding vector $\boldsymbol{z} \in \mathbb{Z}^{M-N+1}$. Moreover, the number of possible winding vectors is finite. From Eq. (24) we see that solutions can be found only if

$$|z_\alpha| \leq \frac{\text{number of edges in cycle } \alpha}{\mathcal{N}_\alpha}, \tag{25}$$

where $\mathcal{N}_\alpha$ denotes the number of edges in the cycle α. Generalizations of this approach to power grids with Ohmic losses have been proposed in Refs. [26,27].

A summary of the symbols and variables used in this article is provided in Table I to improve readability.

IV. REAL POWER FLOW FROM OPTIMIZATION

In this section, we introduce a convex optimization–based formulation of the nonlinear real power flow

TABLE I. List of symbols and variables. Vectors are written as boldface lowercase Roman letters and matrices are written as boldface uppercase Roman letters. Calligraphic letters are used to denote objective and Lagrangian functions, while Gothic-type letters denote sets and graphs.

Symbol or variable	Definition
e, a, b	Indices of lines or edges
α, β, φ	Indices of (fundamental) cycles
$C_{e\beta}$	Entry of the edge-cycle incidence matrix
$\boldsymbol{C}$	Edge-cycle incidence matrix
$\mathfrak{E}$	Set of all lines or edges in the grid
E_{ne}	Entry of the node-edge incidence matrix
$\boldsymbol{E}$	Node-edge incidence matrix
f_e	Real power flow on line e
$\mathcal{F}$	Objective function
$\boldsymbol{f}$	Vector of all real-power flows
$\mathfrak{G}$	Graph or network
K_e	Coupling strength of a line e (proportional to the inverse of the reactance X_e^{-1})
$\boldsymbol{K}$	Diagonal matrices of coupling constants
l, m, n	Indices of nodes
$\boldsymbol{L}$	Laplacian matrix
$\mathcal{L}$	Lagrange function
ℓ_β	Loop flow amplitude on the cycle β
$\boldsymbol{\ell}$	Vector of all loop flow amplitudes
p_n	Real power injection at node n
$\boldsymbol{p}$	Vector of all real power injections
θ_n	Voltage phase angle at node n
$\mathfrak{V}$	Set of all nodes or vertices in the grid

equations

$$p_n = \sum_{m\in\mathfrak{V}} K_{nm} \sin(\theta_n - \theta_m) \text{ for all } m \in \mathfrak{V}. \quad (26)$$

We demonstrate that this approach allows us to compute *all* normal solutions, and we discuss several approximation schemes. Notably, our approach focuses on the lines and cycles of the grid instead of the nodes.

A. Solutions by convex optimization

We consider the optimization problem

$$\min_{\boldsymbol{f}} \quad \mathcal{F}_{\mathrm{RP}}(\boldsymbol{f}) \quad (27)$$

$$\text{subject to} \quad -K_e \le f_e \le K_e \text{ for all } e \in \mathfrak{E}, \quad (28)$$

$$p_n = \sum_e E_{ne} f_e \text{ for all } n \in \mathfrak{V} \quad (29)$$

with the objective function

$$\mathcal{F}_{\mathrm{RP}}(\boldsymbol{f}) = \sum_{e\in\mathfrak{E}} f_e \arcsin\left(\frac{f_e}{K_e}\right) + \sqrt{K_e^2 - f_e^2} - K_e. \quad (30)$$

We note that the objective function is a sum over the edges in the network without any interaction terms. Hence, the edge flows f_e are coupled only via the equality constraint. This particular form simplifies the analysis of the objective function and allows us to derive the following lemma.

Lemma 2. The objective function $\mathcal{F}_{\mathrm{RP}}(\boldsymbol{f})$ is strictly convex for $K_e \le f_e \le K_e$. Hence, the optimization problem (27) either is infeasible or has a unique solution.

Proof. The strict convexity of the objective function is shown by our computing its Hesse matrix. We find that the Hesse matrix $\nabla^2\mathcal{F}_{\mathrm{RP}}$ is diagonal, with all diagonal entries being strictly positive:

$$\frac{\partial^2 \mathcal{F}_{\mathrm{RP}}}{\partial f_a \partial f_b} = \begin{cases} (K_a^2 - f_a^2)^{-1/2} & \text{for } a = b, \\ 0 & a \neq b. \end{cases}$$

Hence, the objective function is strictly convex.

The feasible space is the intersection of a polytope [defined by Eq. (28)] and an affine space [defined by Eq. (29)] and, therefore, convex. We conclude that the optimization problem either is infeasible or has a unique solution. ■

Theorem 1. If the optimization problem (27) is primarily feasible and the solution satisfies

$$|f_e| < K_e \text{ for all } e \in \mathfrak{E},$$

then the solution coincides with a normal solution of the real power flow equations (26) where the phases θ_n correspond to the Lagrangian multipliers of the problem.

Proof. We solve the optimization problem by introducing the Lagrangian function

$$\mathcal{L}(\boldsymbol{f}) = \mathcal{F}_{\mathrm{RP}}(\boldsymbol{f}) + \sum_{e\in\mathfrak{E}} \mu_e(f_e - K_e) + \sum_{e\in\mathfrak{E}} \nu_e(-f_e - K_e) + \sum_{n\in\mathfrak{V}} \lambda_n \left(p_n - \sum_{e\in\mathfrak{E}} E_{ne} f_e\right).$$

The optimization problem satisfies the Slater condition; hence, every optimum fulfills the Karush-Kuhn-Tucker conditions:

(1) Stationarity with respect to f_e:

$$\frac{\partial \mathcal{L}}{\partial f_e} = \arcsin\left(\frac{f_e}{K_e}\right) + (\mu_e - \nu_e) - \sum_n \lambda_n E_{ne} = 0$$

for all edges $e \in \mathfrak{E}$.

(2) Primal feasibility:

$$-K_e \le f_e \le K_e \text{ for all } e \in \mathfrak{E},$$
$$p_n = \sum_e E_{ne} f_e \text{ for all } n \in \mathfrak{V}.$$

(3) Dual feasibility:

$$\mu_e \ge 0, \quad \nu_e \ge 0 \text{ for all } e \in \mathfrak{E}.$$

(4) Complementary slackness:

$$\mu_e(f_e - K_e) = 0, \quad \nu_e(-f_e - K_e) = 0 \text{ for all } e \in \mathfrak{E}.$$

By assumption we have $|f_e| < K_e$ such that the complementary slackness condition yields $\mu_e = \nu_e = 0$ for all edges $e \in \mathfrak{E}$. The stationarity condition with respect to the variables f_e then reads

$$\arcsin\left(\frac{f_e}{K_e}\right) = \sum_n E_{ne}\lambda_n$$
$$\Leftrightarrow \quad f_e = K_e \sin\left(\sum_n E_{ne}\lambda_n\right),$$

which we substitute into the equality constraint

$$p_m = \sum_{e\in\mathfrak{E}} E_{me} K_e \sin\left(\sum_n E_{ne}\lambda_n\right).$$

Now we switch our notation and label the edges by their respective endpoints. Using the structure of the node-edge incidence matrix, we can recast the last equation into the form

$$p_m = \sum_{n\in\mathfrak{V}} K_{nm} \sin(\lambda_n - \lambda_m).$$

This coincides with the real power flow equations (26) if we identify λ_n and θ_n. ■

Before we proceed, we briefly comment on the assumptions underlying Theorem 1. Throughout this article, we restrict ourselves to normal fixed points, i.e., fixed points that satisfy $|\theta_n - \theta_m| < \pi/2$ and are guaranteed to be dynamically stable. The proposed framework can be partly generalized to describe fixed points violating this condition.

To be more precise, we consider a stationary state with $|\theta_n - \theta_m| > \pi/2$ for a subset of edges $(n,m) \in \mathfrak{E}_-$. For these edges, we can recover the phases from the real power flow f_e using the second option in Eq. (23). For all remaining edges, we assume that $|\theta_n - \theta_m| < \pi/2$ and we define $\mathfrak{E}_+ = \mathfrak{E}\backslash\mathfrak{E}_-$. One can then show that this fixed point is a critical point of the function

$$\mathcal{F}_{\mathrm{sp}}(\boldsymbol{f}) = \sum_{e\in\mathfrak{E}_+} \mathcal{F}_e(f_e) + \sum_{e\in\mathfrak{E}_-} \pi f_e - \mathcal{F}_e(f_e)$$

on the affine subset defined by $\boldsymbol{E}\boldsymbol{f} = \boldsymbol{p}$, where we have defined the shorthand

$$\mathcal{F}_e(f_e) = f_e \arcsin\left(\frac{f_e}{K_e}\right) + \sqrt{K_e^2 - f_e^2}.$$

However, these critical points are typically saddle points, not minima.

B. Multistability

Theorem 1 provides a systematical approach to the real power flow equations and the stationary states of oscillator networks. The optimization problem (27) has either a unique solution or no solution at all. However, we know that the Kuramoto model is generally multistable, i.e., it can have multiple stable fixed points. Can we get them all by convex optimization?

As stressed above, we restrict ourselves to normal-operation fixed points for the time being. The following analysis is based on the cycle decomposition reviewed in Sec. III and the results in Ref. [20]. We have shown that all solutions of the real power flow equations can be obtained from the general solution of KCL

$$\boldsymbol{f} = \boldsymbol{f}^{(0)} + \boldsymbol{C}\boldsymbol{\ell},$$

where $\boldsymbol{f}^{(0)}$ denotes a special solution of KCL—for instance, the one that is obtained from solving the optimization problem (27). Then the cycle flow amplitudes $\boldsymbol{\ell}$ must satisfy the conditions

$$\sum_e C_{e\beta} \arcsin\left(\frac{f_e}{K_e}\right) = 2\pi z_\beta \tag{31}$$

for all fundamental cycles β. Notably, the winding vector $\boldsymbol{z} = (z_1, \ldots, z_{M-N+1})$ is unique for every fixed point, as discussed above. Hence, we can actually try to define a specific convex optimization problem for a given $\boldsymbol{z}$, whose unique solution then reproduces the condition (31). Indeed, this is possible as we show now.

Consider the optimization problem

$$\min_{\boldsymbol{\ell}} \quad \mathcal{F}_z(\boldsymbol{\ell})$$
$$\text{subject to} \quad -K_e \le f_e^{(0)} + \sum_\beta C_{e\beta}\ell_\beta \le K_e \text{ for all } e \in \mathfrak{E} \tag{32}$$

with the objective function

$$\mathcal{F}_z(\boldsymbol{\ell}) = \sum_{e\in\mathfrak{E}} \sqrt{K_e^2 - (f_e^{(0)} + \sum_\beta C_{e\beta}\ell_\beta)^2} - K_e + \sum_{e\in\mathfrak{E}} \left(f_e^{(0)} + \sum_\beta C_{e\beta}\ell_\beta\right) \arcsin\left(\frac{f_e^{(0)} + \sum_\beta C_{e\beta}\ell_\beta}{K_e}\right) - \sum_\beta 2\pi z_\beta \ell_\beta. \tag{33}$$

Lemma 3. The optimization problem (32) either is infeasible or has a unique solution.

Proof. The feasible space is the intersection of a polytope and an affine space and, therefore, convex (or empty). The objective function is strictly convex. To prove this statement, we compute the Hesse matrix

$$\frac{\partial \mathcal{F}_z}{\partial \ell_\alpha} = \sum_e C_{e\alpha} \arcsin\left(\frac{f_e^{(0)} + \sum_\varphi C_{e\varphi}\ell_\varphi}{K_e}\right) - 2\pi z_\alpha$$

$$\frac{\partial^2 \mathcal{F}_z}{\partial \ell_\alpha \partial \ell_\beta} = \sum_e \frac{C_{e\alpha}C_{e\beta}}{\sqrt{K_e^2 - (f_e^{(0)} + \sum_\varphi C_{e\varphi}\ell_\varphi)^2}}.$$

Converting this result to a matrix form, we find that the Hesse matrix reads

$$\nabla^2 \mathcal{F}_z = \boldsymbol{C}^\top \mathrm{diag}\left(\frac{1}{\sqrt{K_e^2 - (f_e^{(0)} + \sum_\varphi C_{e\varphi}\ell_\varphi)^2}}\right) \boldsymbol{C}. \tag{34}$$

We see that the Hesse matrix is positive definite on the interior of the feasible set where

$$\left|f_e^{(0)} + \sum_\beta C_{e\beta}\ell_\beta\right| < K_e,$$

whereas it becomes singular on the boundary. We conclude that the optimization problem either is infeasible or has a unique solution. ■

Theorem 2. If the optimization problem (32) is primarily feasible and the solution satisfies

$$|f_e^{(0)} + \sum_\beta C_{e\beta}\ell_\beta| < K_e \text{ for all } e \in \mathfrak{E},$$

then the solution coincides with a normal solution of the real power flow equations (26) with the winding vector $\boldsymbol{z} = (z_1, \ldots, z_{M-N+1})$.

Proof. We solve the optimization problem by introducing the Lagrangian function

$$\mathcal{L}(\boldsymbol{\ell}) = \mathcal{F}_z(\boldsymbol{\ell}) + \sum_{e\in\mathfrak{E}} \mu_e \left(f_e^{(0)} + \sum_\beta C_{e\beta}\ell_\beta - K_e\right) + \sum_{e\in\mathfrak{E}} \nu_e \left(-f_e^{(0)} - \sum_\beta C_{e\beta}\ell_\beta - K_e\right).$$

The optimization problem satisfies the Slater condition; hence, every optimum fulfills the Karush-Kuhn-Tucker conditions:

(1) Stationarity with respect to ℓ_α:

$$0 = \frac{\partial \mathcal{L}}{\partial \ell_\alpha} = -2\pi z_\alpha + \sum_e C_{e\alpha}\left[\arcsin\left(\frac{f_e^{(0)} + \sum_\beta C_{e\beta}\ell_\beta}{K_e}\right) + (\mu_e - \nu_e)\right]$$

for all fundamental cycles β.

(2) Primal feasibility:

$$-K_e \le f_e^{(0)} + \sum_\beta C_{e\beta}\ell_\beta \le K_e.$$

(3) Dual feasibility:

$$\mu_e \ge 0, \quad \nu_e \ge 0 \text{ for all } e \in \mathfrak{E}.$$

(4) Complementary slackness:

$$\mu_e \left(f_e^{(0)} + \sum_\beta C_{e\beta}\ell_\beta - K_e\right) = 0,$$

$$\nu_e \left(-f_e^{(0)} - \sum_\beta C_{e\beta}\ell_\beta - K_e\right) = 0 \text{ for all } e \in \mathfrak{E}.$$

By assumption we have $|f_e^{(0)} + \sum_\beta C_{e\beta}\ell_\beta| < K_e$ for all $e \in \mathfrak{E}$ such that the complementary slackness condition yields $\mu_e = \nu_e = 0$ for all edges $e \in \mathfrak{E}$. The stationarity condition with respect to the variables ℓ_α then reads

$$\sum_{e=1}^{M} C_{e\alpha} \arcsin\left(\frac{f_e^{(0)} + \sum_{\beta=1}^{M-N+1} C_{e\beta}\ell_\beta}{K_e}\right) = 2\pi z_\alpha. \tag{35}$$

Hence, the solution of the optimization problem satisfies the two conditions for the normal solution of the real power

flow equations given in Sec. III. First, it satisfies KCL by construction. Second, the stationarity condition (35) coincides with the cycle condition (24). ■

We close this section with three remarks on the implications of the two theorems established above. First, the optimization problem (27) yields a solution with winding vector $\boldsymbol{z} = \boldsymbol{0}$ (or no suitable solution at all). To see this, we use this solution as the reference $\boldsymbol{f}^{(0)}$ in the optimization problem (32) with $\boldsymbol{z} = \boldsymbol{0}$. Then the minimizer is simply given by $\boldsymbol{\ell} = \boldsymbol{0}$. Hence, the solution $\boldsymbol{f}^\star = \boldsymbol{f}^{(0)} + \boldsymbol{C}\boldsymbol{\ell} = \boldsymbol{f}^{(0)}$ has the winding number $\boldsymbol{z} = \boldsymbol{0}$. Normal solutions with $\boldsymbol{z} = 0$ are by far the most important ones in practice—all other ones correspond to rather exotic states with loop flows; see Ref. [43] for a discussion.

Second, we emphasize that Theorem 2 provides a systematic approach to compute *all* normal solutions of the real power flow equations (26). More precisely, we can find the following scenarios:

(1) Given the network and the real power injections $\boldsymbol{p}$, the optimization problems may be infeasible. That is, there is no solution of KCL $\boldsymbol{E}\boldsymbol{f} = \boldsymbol{p}$ that satisfies the line limits $|f_e| \leq K_e$. In this case, the grid simply does not have enough capacity to transmit the power from generators to consumers. Whether this is the case can be determined in a systematic way by graph-theoretic methods; see Appendix A.

(2) If there is a solution $\boldsymbol{f}^{(0)}$ of KCL satisfying the line limits, then the optimization problem (32) has a unique solution for each winding vector $\boldsymbol{z}$. As the winding vector is unique, we can hence systematically compute the respective solution and also decide whether it exists at all by distinguishing three cases:

   (a) If the solution is in the interior of the feasible set (i.e., $|f_e| < K_e$ for all lines e), then we have found the correct solution for the given $\boldsymbol{z}$.
   (b) If the solution lies on the boundary of the feasible space (i.e., $|f_e| = K_e$ for at least one line e), then generally, no solution with the given winding vector $\boldsymbol{z}$ exists.
   (c) In a special case, we may find a solution with $|f_e| = K_e$ where the respective Karush-Kuhn-Tucker multiplier (μ_e or ν_e) vanishes too. Then we have found a valid solution of the real power flow equations. This case typically corresponds to a bifurcation point, where the solution will vanish on the variation of a system parameter.

   A different algorithm based on a contraction mapping was proposed in Ref. [20].

(3) To systematically compute all possible solutions, one further needs information about the set of possible winding vectors $\boldsymbol{z}$. A comprehensive characterization of the possible winding vectors is given in Ref. [20], including an upper bound on the number of possible vectors. Scaling arguments for the number of possible vectors were presented in Ref. [16].

Finally, we remark that the suggested procedure to compute all normal solutions may still be computationally hard, depending on the topology of the network. For every fundamental cycle α, the number of allowed values z_α is finite according to Eq. (25). The number of allowed winding vectors $\boldsymbol{z}$ is thus also finite, but it can grow exponentially with the number of cycles.

V. THE LINEAR POWER FLOW APPROXIMATION

The linear power flow or dc approximation is widely used in practical approximations. Here, one simply linearizes the sine function in Eq. (26) and obtains a system of linear equations

$$p_n = \sum_{m \in \mathfrak{V}} K_{nm}(\theta_n - \theta_m) \text{ for all } m \in \mathfrak{V} \tag{36}$$

that is easily solved for the nodal phase angles as discussed in Sec. III. Here we discuss how this approximation relates to our optimization approach and how this approximation may be refined.

A. The linear power flow as an optimization problem

We first note that the linear power flow equations can also be obtained from a convex optimization problem:

$$\begin{aligned} \min_{\boldsymbol{f}} \quad & \mathcal{F}_{\text{lin}}(\boldsymbol{f}) \\ \text{subject to} \quad & p_n = \sum_e E_{ne} f_e \text{ for all } n \in \mathfrak{V} \end{aligned} \tag{37}$$

with the objective function

$$\mathcal{F}_{\text{lin}}(\boldsymbol{f}) = \sum_{e \in \mathfrak{E}} \frac{f_e^2}{2K_e}. \tag{38}$$

To see this, we introduce the Lagrangian

$$\mathcal{L}(\boldsymbol{f}) = \mathcal{F}_{\text{lin}}(\boldsymbol{f}) + \sum_{n \in \mathfrak{V}} \lambda_n \left(p_n - \sum_{e \in \mathfrak{E}} E_{ne} f_e \right).$$

The stationarity condition with respect to f_e then reads

$$\frac{\partial \mathcal{L}}{\partial f_e} = \frac{f_e}{K_e} - \sum_n \lambda_n E_{ne} = 0$$

for all edges $e \in \mathfrak{E}$. Substituting this result into the equality constraints, we obtain

$$p_m = \sum_{e\in\mathfrak{E}} E_{me} K_e \left(\sum_n E_{ne} \lambda_n \right).$$

Switching our notation and labeling the edges by their respective endpoints, we can recast this equation into the form

$$p_m = \sum_{n\in\mathfrak{V}} K_{nm} (\lambda_n - \lambda_m).$$

This coincides with the linear power flow equations (36) if we identify λ_n and θ_n.

Now, how does the optimization problem (37) relate to the previous problem (27)? By straightforward computation, one can show that the objective function $\mathcal{F}_{\rm lin}$ is the leading-order Taylor expansion of the original objective function $\mathcal{F}_{\rm RP}$ around the "empty grid" $\boldsymbol{f} = \mathbf{0}$:

$$\mathcal{F}_{\rm RP}(\boldsymbol{f}) = \mathcal{F}_{\rm lin}(\boldsymbol{f}) + \mathcal{O}({f_e}^4).$$

Furthermore, the optimization problem (37) neglects the inequality constraints, i.e., the line limits.

B. Improving on the linear power flow approximation

The previous insights provide a method to improve the linear power flow approximation. In the first step we linearize the objective function $\mathcal{F}_{\rm RP}(\boldsymbol{f})$ around $\boldsymbol{f} = \mathbf{0}$ and obtain the linear power flow $\boldsymbol{f}^{\rm (lin)}$. Alternatively, we can linearize the objective $\mathcal{F}_{\boldsymbol{z}=\mathbf{0}}(\boldsymbol{\ell})$ around $\boldsymbol{\ell} = \mathbf{0}$. We can repeat this idea and do another Taylor expansion, but this time around the previous approximate solution $\boldsymbol{f}^{\rm (lin)}$.

Let us evaluate this idea. The linear power flow providing the starting point is given by

$$\begin{aligned} \boldsymbol{\theta}^{\rm (lin)} &= \boldsymbol{L}^{+}\boldsymbol{p}, \\ \boldsymbol{f}^{\rm (lin)} &= \boldsymbol{K}\boldsymbol{E}^{\top}\boldsymbol{\theta}^{\rm (lin)}. \end{aligned} \tag{39}$$

For a given edge $e = (n, m)$, we further define $\theta_e^{\rm (lin)} = \theta_n^{\rm (lin)} - \theta_m^{\rm (lin)}$. Furthermore, we use the Taylor expansion of the objective function. Writing $f_e = {f_e}^{\rm (lin)} + \Delta f_e$, we obtain

$$\begin{aligned} & f_e \arcsin\left(\frac{f_e}{K_e}\right) + \sqrt{K_e^2 - {f_e}^2} - K_e \\ &= {f_e}^{\rm (lin)} \arcsin\left(\frac{{f_e}^{\rm (lin)}}{K_e}\right) + \sqrt{K_e^2 - {f_e}^{\rm (lin)2}} - K_e \\ &+ \arcsin\left(\frac{{f_e}^{\rm (lin)}}{K_e}\right) \Delta f_e + \frac{1}{\sqrt{K_e^2 - {f_e}^{\rm (lin)2}}} \Delta {f_e}^2 + \mathcal{O}(\Delta {f_e}^3). \end{aligned}$$

Now we can rewrite the optimization problem (32). If we set $\Delta\boldsymbol{f} = \boldsymbol{C}\boldsymbol{\ell}$, the objective function reads

$$\begin{aligned} \mathcal{F}_{z=\mathbf{0}}(\boldsymbol{\ell}) = & \sum_{e\in\mathfrak{E}} {f_e}^{\rm (lin)} \arcsin\left(\frac{{f_e}^{\rm (lin)}}{K_e}\right) + \sqrt{K_e^2 - {f_e}^{\rm (lin)2}} \\ & - K_e + \sum_{e\in\mathfrak{E}} \arcsin\left(\frac{{f_e}^{\rm (lin)}}{K_e}\right) \sum_\beta C_{e\beta}\ell_\beta \\ & + \sum_{e\in\mathfrak{E}} \frac{1}{\sqrt{K_e^2 - {f_e}^{\rm (lin)2}}} \left(\sum_\beta C_{e\beta}\ell_\beta\right)^2 + \mathcal{O}(\ell^3). \end{aligned}$$

We ignore the inequality constraints for the time being, as in the linear power flow approximation, and discard the higher-order terms. The minimizer is then found by our requiring the objective to be stationary:

$$\begin{aligned} 0 = \frac{\partial \mathcal{F}_{z=0}}{\partial \ell_\alpha} = & \sum_e \arcsin\left(\frac{{f_e}^{\rm (lin)}}{K_e}\right) C_{e\alpha} \\ & + \sum_{e,\beta} \frac{1}{\sqrt{K_e^2 - {f_e}^{\rm (lin)2}}} C_{e\alpha} C_{e\beta} \ell_\beta. \end{aligned}$$

Using the explicit forms of the gradient and the Hessian for the optimization problem (27), we rewrite this set of linear equations in vectorial notation:

$$\left(\boldsymbol{C}^\top \nabla^2 \mathcal{F}_{\rm RP}(\boldsymbol{f}^{\rm (lin)})\boldsymbol{C}\right)\boldsymbol{\ell} = -\boldsymbol{C}^\top \nabla \mathcal{F}_{\rm RP}(\boldsymbol{f}^{\rm (lin)}),$$

which is readily solved for $\boldsymbol{\ell}$. We thus obtain an approximate solution of the nonlinear real power flow equation,

$$\begin{aligned} \boldsymbol{f}^{\rm (approx)} &= \boldsymbol{f}^{\rm (lin)} + \boldsymbol{C}\boldsymbol{\ell} \\ &= \boldsymbol{f}^{\rm (lin)} - \boldsymbol{C}\left[\boldsymbol{C}^\top \nabla^2 \mathcal{F}_{\rm RP}(\boldsymbol{f}^{\rm (lin)})\boldsymbol{C}\right]^{-1} \\ &\quad \cdot \boldsymbol{C}^\top \nabla \mathcal{F}_{\rm RP}(\boldsymbol{f}^{\rm (lin)}). \end{aligned} \tag{40}$$

Notably, this expression is no longer linear in the power injections $\boldsymbol{p}$. Nevertheless, it provides an explicit formula for the flows $\boldsymbol{f}^{\rm (approx)}$ in closed form.

To evaluate the quality of our improved approximation of the real power flow, we compare the errors of the purely linear approximation with the errors of our improved approximation for a simple 30-bus test case and for $\boldsymbol{z} = 0$; see Fig. 1. In this calculation, we used the minimal cycle base of the network. For the heavily loaded test grid, our approximation reduces the median of the approximation errors by at least 3 orders of magnitude and the error on the heaviest loaded line by 2 orders of magnitude. For a grid with small loads, the reduction is up to 9 orders of magnitude.

Since the correction term can be calculated purely algebraically and, in particular, reduces the errors on the

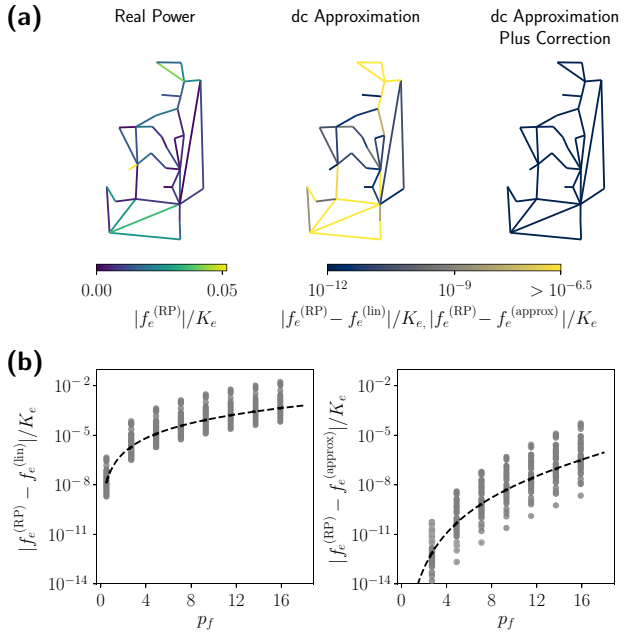

FIG. 1. Assessment of the improved power flow approximation (40). We compute the real power flows $\boldsymbol{f}$ for an adapted MATPOWER 30-bus test case (see Appendix E) and compare numerically exact values $\boldsymbol{f}^{(\mathrm{RP})}$ with the linear (dc) approximation $\boldsymbol{f}^{(\mathrm{lin})}$ and the improved approximation $\boldsymbol{f}^{(\mathrm{approx})}$ given by Eq. (40). (a) The left panel shows the loading $|f_e^{(\mathrm{RP})}|/K_e$ for each edge e for the exact solution. The other two panels depict the errors $|f_e^{(\mathrm{RP})} - f_e^{(\mathrm{lin})}|/K_e$ and $|f_e^{(\mathrm{RP})} - f_e^{(\mathrm{approx})}|/K_e$, respectively, of the linear approximation (middle) and the improved approximation (right). Errors are hardly visible for the improved approximation (40), even on a logarithmic scale. (b) For a systematic assessment, we increase the overall grid load by multiplying all power injections by a scaling factor p_f. The panels show the error on all edges as a function of p_f in a scatter plot for the linear approximation (left) and the improved approximation (right). The improved approximation (40) reduces the error on most edges by at least 2 orders of magnitudes for $p_f = 20$ and by up to 9 orders of magnitude for $p_f = 1$. For $p_f = 1$, the errors of the improved approximation are below 10^{-14}, approaching the numerical precision.

heavily loaded lines, this improved approximation can be of interest for any application where running a full load flow consumes too many resources (e.g., in contingency analysis).

The procedure described above can be viewed as one step in Newton's algorithm restricted to the linear subspace defined by KCL. This step can be generalized to arbitrary values of $\boldsymbol{z}$ and iterated to obtain an explicit tailored algorithm to solve the optimization problems (27) and (32). We discuss this algorithm in more detail in Appendix B.

C. Bounding the error in the linear power flow approximation

We may use our insights to bound the error introduced by the linear power flow approximation. That is, we derive a bound on the norm of the difference between real and linear power solutions,

$$\boldsymbol{\xi} = \boldsymbol{f}^{(\mathrm{RP})} - \boldsymbol{f}^{(\mathrm{lin})}. \tag{41}$$

To formulate the bound, we define the function

$$\mathcal{G}(\boldsymbol{f}) := \mathcal{F}_{\mathrm{RP}}(\boldsymbol{f}) - \mathcal{F}_{\mathrm{lin}}(\boldsymbol{f}). \tag{42}$$

Decomposing this function into components $\mathcal{G}(\boldsymbol{f}) = \sum_e \mathcal{G}_e(f_e)$, we have

$$\mathcal{G}_e(f_e) = f_e \arcsin\left(\frac{f_e}{K_e}\right) + \sqrt{K_e^2 - f_e^2} - K_e - \frac{f_e^2}{2K_e},$$
$$\mathcal{G}_e'(f_e) = \arcsin\left(\frac{f_e}{K_e}\right) - \frac{f_e}{K_e},$$

where the prime denotes the derivative with respect to the argument. One can see that $\mathcal{G}_e(f_e) \ll 1$ if the loads are small, $f_e \ll K_e$. Furthermore, we define the vector $\boldsymbol{\zeta}$ with components

$$\zeta_e = K_e \mathcal{G}_e'(f_e^{(\mathrm{lin})}). \tag{43}$$

We then obtain the following bound for the deviation of real and linear power flow.

Theorem 3. Let $\boldsymbol{f}^{(\mathrm{RP})}$ denote the solution of the real power flow equations with $\boldsymbol{z} = \boldsymbol{0}$ and $\boldsymbol{f}^{(\mathrm{lin})}$ the solution of the linear power flow equations, assuming that both satisfy $|f_e| < K_e$. Then the difference

$$\boldsymbol{\xi} = \boldsymbol{f}^{(\mathrm{RP})} - \boldsymbol{f}^{(\mathrm{lin})} \tag{44}$$

is bounded as

$$\|\boldsymbol{\xi}\|_K \le \|\boldsymbol{\zeta}\|_K = \left[\sum_e K_e \mathcal{G}_e'(f_e^{(\mathrm{lin})})^2\right]^{1/2}, \tag{45}$$
$$\|\boldsymbol{\xi}\|_K \le \|\boldsymbol{\Pi}_{\mathrm{cycle}}\boldsymbol{\zeta}\|_K, \tag{46}$$

where we used the inner product (19) and the associated norm $\|\boldsymbol{\xi}\|_K^2 := \langle \boldsymbol{\xi}, \boldsymbol{\xi}\rangle_K$.

Proof. We have

$$\mathcal{F}_{\mathrm{RP}}(\boldsymbol{f}^{(\mathrm{RP})}) = \mathcal{F}_{\mathrm{lin}}(\boldsymbol{f}^{(\mathrm{lin})} + \boldsymbol{\xi}) + \mathcal{G}(\boldsymbol{f}^{(\mathrm{lin})} + \boldsymbol{\xi}).$$

We can rewrite the first term as

$$\mathcal{F}_{\mathrm{lin}}(\boldsymbol{f}^{(\mathrm{lin})} + \boldsymbol{\xi}) = \frac{1}{2}\|\boldsymbol{f}^{(\mathrm{lin})} + \boldsymbol{\xi}\|_K^2$$
$$= \mathcal{F}_{\mathrm{lin}}(\boldsymbol{f}^{(\mathrm{lin})}) + \frac{1}{2}\|\boldsymbol{\xi}\|_K^2$$

since $\langle \boldsymbol{\xi}, \boldsymbol{f}^{(\mathrm{lin})}\rangle_K = 0$ for all $\boldsymbol{\xi}$ in the kernel of $\boldsymbol{E}$. Using the first-order Taylor expansion of the function $\mathcal{G}_e$ and the fact

that the function is convex, we can bound the second term from below:

$$\mathcal{G}(\boldsymbol{f}^{(\mathrm{lin})}+\boldsymbol{\xi}) \geq \sum_e \mathcal{G}_e(f_e^{(\mathrm{lin})}) + \mathcal{G}_e'(f_e^{(\mathrm{lin})})\xi_e.$$

We thus obtain

$$\mathcal{F}_{\mathrm{RP}}(\boldsymbol{f}^{(\mathrm{RP})}) \geq \mathcal{F}_{\mathrm{RP}}(\boldsymbol{f}^{(\mathrm{lin})}) + \frac{1}{2}\|\boldsymbol{\xi}\|_K^2 + \langle \boldsymbol{\zeta}, \boldsymbol{\xi}\rangle_K. \tag{47}$$

On the other hand, the vector $\boldsymbol{f}^{(\mathrm{RP})}$ is the minimizer of the function $\mathcal{F}_{\mathrm{RP}}$ by definition such that $\mathcal{F}_{\mathrm{RP}}(\boldsymbol{f}^{(\mathrm{lin})}) \geq \mathcal{F}_{\mathrm{RP}}(\boldsymbol{f}^{(\mathrm{RP})})$. Applying Taylor's theorem as detailed in Appendix C, we can obtain the bound

$$\mathcal{F}_{\mathrm{RP}}(\boldsymbol{f}^{(\mathrm{lin})}) \geq \mathcal{F}_{\mathrm{RP}}(\boldsymbol{f}^{(\mathrm{RP})}) + \frac{1}{2}\|\boldsymbol{\xi}\|_K^2. \tag{48}$$

Combining this inequality with the inequality (47), we conclude that

$$\|\boldsymbol{\xi}\|_K^2 + \langle \boldsymbol{\zeta}, \boldsymbol{\xi}\rangle_K \leq 0. \tag{49}$$

Applying the Cauchy-Schwarz inequality, we obtain Eq. (45).

To obtain the second bound, we note that $\boldsymbol{\xi}$ is a pure cycle flow because $\boldsymbol{f}^{(\mathrm{lin})}$ and $\boldsymbol{f}^{(\mathrm{RP})}$ both satisfy KCL. Hence, we find that $\boldsymbol{\xi} = \boldsymbol{\Pi}_{\mathrm{cycle}}\boldsymbol{\xi}$. Using the orthogonality of the projection with respect to the inner product (19), we can rewrite the inequality (49) and obtain

$$\begin{aligned} 0 &\geq \frac{1}{2}\|\boldsymbol{\xi}\|_K^2 + \langle \boldsymbol{\zeta}, \boldsymbol{\xi}\rangle_K \\ &= \frac{1}{2}\|\boldsymbol{\xi}\|_K^2 + \langle \boldsymbol{\zeta}, \boldsymbol{\Pi}_{\mathrm{cycle}}\boldsymbol{\xi}\rangle_K \\ &= \frac{1}{2}\|\boldsymbol{\xi}\|_K^2 + \langle \boldsymbol{\Pi}_{\mathrm{cycle}}\boldsymbol{\zeta}, \boldsymbol{\xi}\rangle_K. \end{aligned}$$

Applying the Cauchy-Schwarz inequality and squaring the result, we obtain Eq. (46). ■

We numerically test the tightness of the derived bounds. To this end, we start from the adapted MATPOWER 30-bus test case (see Appendix E), choose the power injections p_n at random, and numerically compute both the real power flow $\boldsymbol{f}^{(\mathrm{RP})}$ and the linear power flow $\boldsymbol{f}^{(\mathrm{lin})}$. Figure 2 shows that the bound (46) incorporating the projection is much tighter than the simpler bound (45).

Theorem 3 provides an upper bound for the K norm of the error $\boldsymbol{\xi}$. We further derive an error bound for every single line, combining the previous result with a general property of cycle flows.

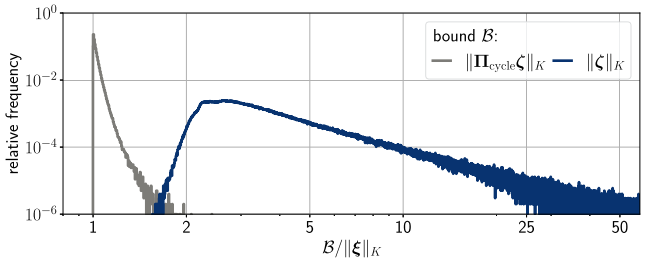

FIG. 2. Assessment of bounds of Theorem 3 for the error of the linear power flow approximation. We solve the real power flow and the linear power flow equations for the adapted MATPOWER 30-bus test case (see Appendix E) and 10^6 randomly sampled and valid power injection vectors $\boldsymbol{p}$. In each case, we compute the norm of error $\|\boldsymbol{\xi}\|_K$ and compare it with the upper bounds given by $\mathcal{B} = \|\boldsymbol{\zeta}\|_K$ and $\mathcal{B} = \|\boldsymbol{\Pi}_{\mathrm{cycle}}\boldsymbol{\zeta}\|_K$, respectively. The figure shows a histogram of the ratio $\mathcal{B}/\|\boldsymbol{\xi}\|_K$, which serves as a measure for the tightness of the bound. The improved upper bound $\|\boldsymbol{\Pi}_{\mathrm{cycle}}\boldsymbol{\zeta}\|_K$ is significantly better and appears to be tight.

Lemma 4. For every cycle flow $\boldsymbol{f}^{(c)}$, i.e., every flow that satisfies $\boldsymbol{E}\boldsymbol{f}^{(c)} = 0$, we have the inequality

$$\|\boldsymbol{f}^{(c)}\|_K^2 \geq \left(f_a^{(c)}\right)^2 \frac{1}{K_a(1-K_a\Omega_a)}$$

for every edge $a = (n,m) \in \mathfrak{E}$, where Ω_a is the effective resistance as defined in Eq. (21).

The proof of this lemma is mostly technical such that we postpone it to Appendix D. We can apply this inequality with Theorem 3, taking into account that $\boldsymbol{E}(\boldsymbol{f}^{(\mathrm{RP})} - \boldsymbol{f}^{(\mathrm{lin})}) = \boldsymbol{0}$. One directly obtains the following error bound.

Corollary 1. For every edge $a = (n,m) \in \mathfrak{E}$, we find that

$$(f_a^{(\mathrm{RP})} - f_a^{(\mathrm{lin})})^2 \leq K_a(1-K_a\Omega_a)\|\boldsymbol{\Pi}_{\mathrm{cycle}}\boldsymbol{\zeta}\|_K^2. \tag{50}$$

VI. GEOMETRY OF REAL AND LINEAR POWER FLOW

We have shown that the real power flow equations and the linear power flow equations can be recast as optimization problems. Comparison of the two objective functions $\mathcal{F}_{\mathrm{RP}}(\boldsymbol{f})$ and $\mathcal{F}_{\mathrm{lin}}(\boldsymbol{f})$ thus provides insights into the relations of the two problems and the limitations of the linear approximation. Here we propose a geometric approach to this topic.

A. Geometric interpretation of the cycle condition

We discussed in Sec. III that the solutions for the real power flow equations are characterized by two conditions: (i) the continuity equation or KCL (13) and (ii) the cycle

condition [see Eq. (24)]

$$\sum_{e=1}^{M} C_{e\alpha} \arcsin\left(\frac{f_e}{K_e}\right) = 2\pi z_\alpha. \tag{51}$$

For the linear power flow equations, the analogue of the cycle condition is given by Kirchhoff's voltage law (KVL):

$$\sum_{e=1}^{M} C_{e\alpha} \left(\frac{f_e}{K_e}\right) = 0. \tag{52}$$

We now discuss how the cycle condition and KVL relate to the optimization problems defined above, restricting ourselves to the case $\boldsymbol{z} = \boldsymbol{0}$ for simplicity. Assuming that the inequality constraints are nonbinding, the solution to a convex optimization problem is found where the gradient of the objective function $\nabla_f \mathcal{F}$ is orthogonal to the linear subspace defined by the equality constraints. This relation is sketched in Fig. 3. In our case, the linear subspace is given by the solutions of KCL and thus is given by all points

$$\boldsymbol{f} = \boldsymbol{f}^{(0)} + \boldsymbol{C\ell},$$

where $\boldsymbol{C\ell}$ is an arbitrary cycle flow.

We now choose a standard unit basis with basis vectors $\boldsymbol{u}_\alpha, \alpha = 1, \ldots, M - N + 1$ for the cycle space. The orthogonality condition of the gradient and the linear subspace is then written as

$$\nabla_f \mathcal{F}(\boldsymbol{f}^\star) \cdot \boldsymbol{C u}_\alpha = 0 \text{ for all } \alpha = 1, \ldots, M - N + 1.$$

Now we can insert the objective function $\mathcal{F}_{\mathrm{RP}}$ or $\mathcal{F}_{\mathrm{lin}}$, compute the gradient, and evaluate the condition. The resulting conditions are nothing but the cycle condition (51) and KVL (52), respectively. Hence, these graph-theoretic conditions have an intuitive geometric interpretation in the context of our optimization problem.

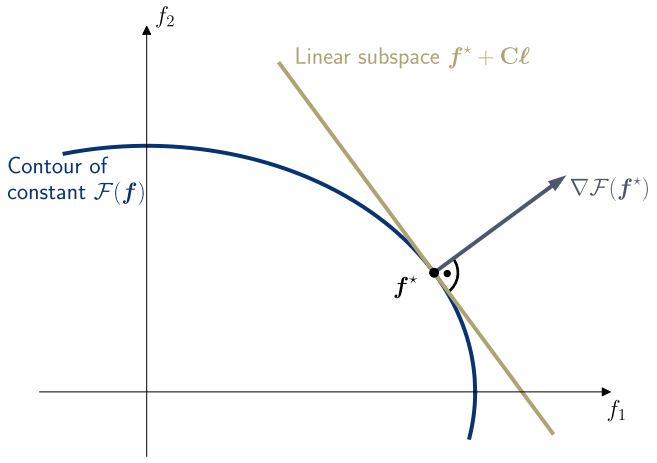

FIG. 3. Geometric interpretation of the cycle conditions. The optimal solution $\boldsymbol{f}^\star$ of the optimization problems (27) and (37) is given by the point where contour lines of the respective objective function $\mathcal{F}(\boldsymbol{f})$ and the linear subspace spanned by the equality constraints $\boldsymbol{Ef} = \boldsymbol{p}$ are tangential. Equivalently, $\boldsymbol{f}^\star$ is the point where the gradient $\nabla\mathcal{F}(\boldsymbol{f})$ is orthogonal to the linear subspace. Since any flow $\boldsymbol{f}$ can be decomposed into directed flow and a cycle flow $\boldsymbol{f}^{(c)} = \boldsymbol{C\ell} \in \ker(\boldsymbol{E})$, the linear subspace is spanned by all points of the form $\boldsymbol{f}^\star + \boldsymbol{C\ell}$.

B. Gradient descent

The geometric interpretation enables another extension of the linear power flow approximation. The linear flows $\boldsymbol{f}^{(\mathrm{lin})}$ provide an easily computable approximation to the real power flows $\boldsymbol{f}^{(\mathrm{RP})}$. In Sec. V B we showed that this approximation can be improved by minimizing $\mathcal{F}_{\mathrm{RP}}$ in the spirit of Newton's method. Instead, we may also minimize $\mathcal{F}_{\mathrm{RP}}$ using a gradient-descent approach. However, we must keep in mind the geometric aspects of the problem: any optimization must take place on the affine linear subspace defined by KCL $\boldsymbol{Ef} = \boldsymbol{p}$. Hence, we cannot simply use the gradient of the objective function $\boldsymbol{\nabla}\mathcal{F}_{\mathrm{RP}}$, but rather need its projection onto the linear subspace. Luckily, Lemma 1 shows how to implement this projection. The gradient-descent step is thus given by

$$\boldsymbol{f}' = \boldsymbol{f} - \gamma \boldsymbol{\Pi}_{\mathrm{cycle}} \boldsymbol{\nabla}\mathcal{F}_{\mathrm{RP}}(\boldsymbol{f}), \tag{53}$$

where γ is the step size. Notably, the gradient is given by

$$\boldsymbol{\nabla}\mathcal{F}_{\mathrm{RP}}(\boldsymbol{f}) = \arcsin(\boldsymbol{K}^{-1}\boldsymbol{f}), \tag{54}$$

where the arcsine is taken elementwise.

We now provide a numerical example and evaluate the gradient-descent step (53) for an adapted MATPOWER 30-bus test case (see Appendix E). The optimal step size $\gamma^\star$ for only one step can be found numerically (see Fig. 4). With one optimal gradient-descent step, the error between the approximated line flows and the real power flows $\boldsymbol{f}^{(\mathrm{RP})}$ is reduced as expected. In particular, the error on the heaviest loaded line is reduced. However, the optimal step size depends on the power injections and the topology of the grid, and is not known *a priori*. One may iterate the gradient-descent step, where appropriate values of γ may be determined by a line search or more advanced methods [44]. As an alternative, one may resort to Newton's method introduced in Sec. V B, which provides good results in a single step.

At this point, we emphasize another application beyond numerical optimization. Given the linear power flow approximation, we can heuristically predict *how* this approximation misses the nonlinear solution. In almost all cases, the first gradient-descent step (53) will point in the

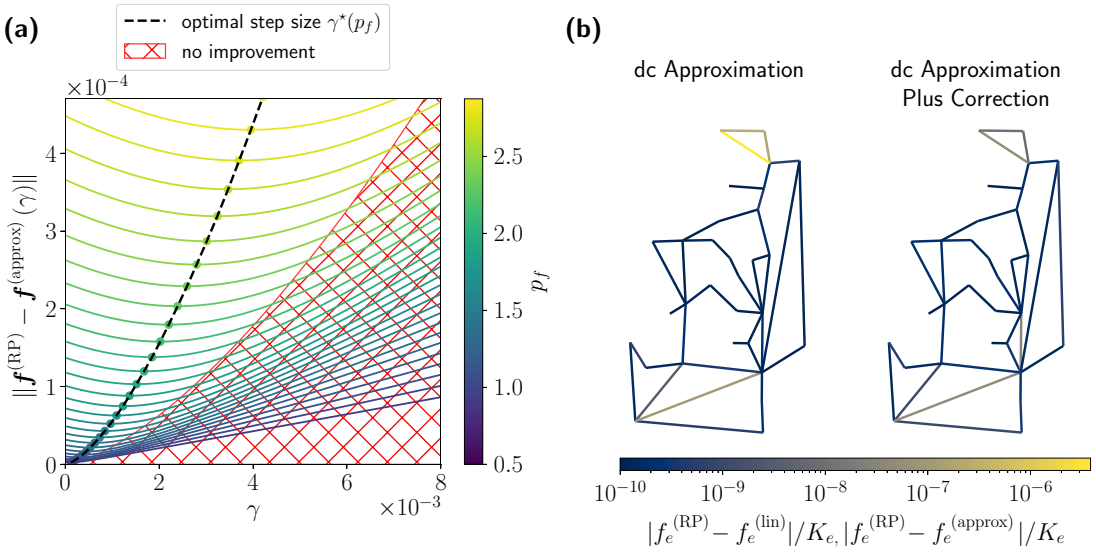

FIG. 4. Improving the linear power flow approximation with the use of a projected gradient descent. We compute the real power flows $\boldsymbol{f}$ for an adapted MATPOWER 30-bus test case (see Appendix E) and compare numerically exact values $\boldsymbol{f}^{(\mathrm{RP})}$ with the improved approximation given by Eq. (53). (a) Error of the approximation as a function of the step size γ for different values of the scaling factor p_f that controls the grid load. The optimal step size $\gamma^\star$, drawn as a dotted black line, increases with p_f. The hatched red area shows where the gradient-descent step does not improve the approximation. (b) Maps depicting the error of the approximation $|f_e^{(\mathrm{RP})} - f_e^{(\mathrm{lin})}|/K_e$, $|f_e^{(\mathrm{RP})} - f_e^{(\mathrm{approx})}|/K_e$ for each individual line e, comparing the linear approximation and the improved approximation given by Eq. (53) for the optimal step size $\gamma^\star$ and $p_f = 1.028$.

correct direction. That is, $\left[\boldsymbol{\Pi}_{\mathrm{cycle}} \nabla \mathcal{F}_{\mathrm{RP}}(\boldsymbol{f}^{(\mathrm{lin})})\right]_e > 0$ typically implies that $f_e^{(\mathrm{RP})} < f_e^{(\mathrm{lin})}$. These heuristics may be used to assess the robustness of the linear power flow: Assume that a line e is almost fully loaded in the linear power flow approximation, $f_e^{(\mathrm{lin})} \approx K_e$. The heuristics then show whether the flow $f_e^{(\mathrm{RP})}$ is higher or lower and thus indicate a potential overload.

C. Properties of real and linear power flows: Examples

The geometric interpretation of the optimization problem allows further insights into the properties of the power flows, in particular the relation of the real power flow equations and the linear power flow approximation. We first consider a simple example as sketched in Fig. 5(a). For simplicity, we assume that all transmission lines have $K_e = 1$. Exploiting the symmetry of the problem, we have only two independent variables f_1 and f_2 that have to satisfy the constraint

$$f_1 + 2f_2 = \bar{p}. \tag{55}$$

The physical flows are found by our minimizing the objective

$$\mathcal{F}_{\mathrm{RP}}(f_1, f_2) = f_1 \arcsin(f_1) + \sqrt{1 - f_1^2} + 4f_2 \arcsin(f_2) + 4\sqrt{1 - f_2^2} - 5. \tag{56}$$

If we instead invoked the linear power flow equation, we would have

$$\mathcal{F}_{\mathrm{lin}}(f_1, f_2) = f_1^2 + 4f_2^2. \tag{57}$$

The two optimization problems are illustrated in Fig. 5(b). Notably, the constraint (55) defines an affine linear subspace, which is shown as a straight line in the Fig. 5(b). The minimizer is found where this affine subspace is *tangent* to the surface of constant $\mathcal{F}(f_1, f_2)$. Comparing real and linear power, we see that the surface of constant $\mathcal{F}_{\mathrm{RP}}$ is more "angled" than the surface of constant $\mathcal{F}_{\mathrm{lin}}$. Hence, the minimizer $\vec{f}^{\,(\mathrm{lin})}$ is closer to one of the axes than the minimizer $\vec{f}^{\,(\mathrm{RP})}$. That is, the real power flows f_1 and f_2 are more balanced than predicted by the linear power flow approximation. Similar geometric arguments apply to many real or linear power flow problems. By comparing the real power flow with the linear power flow approximation, we conclude that flows are *typically* more evenly distributed and the maximum loading is lower. We note that this topic was addressed in Ref. [1], leading to an efficient synchronization condition.

However, one must be careful in formalizing and generalizing these statements. While they are often true, they do not hold in every case. To gain further insights, we conduct a numerical experiment comparing the maximum load $\max_e |f_e|/k_e$ in the real power flow and in the linear approximation. For this experiment, we investigate cyclic

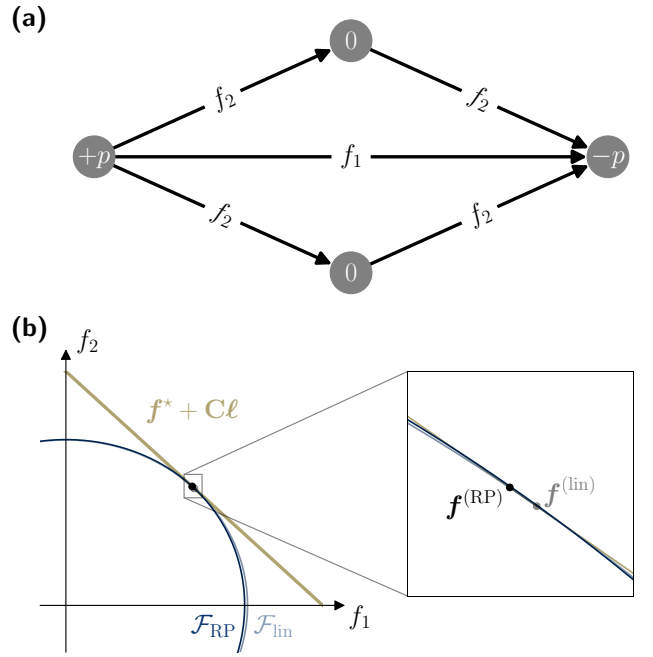

FIG. 5. Geometry of the optimization problems associated with the real power flow and the linear power flow approximation. (a) We consider an elementary four-node network with a high degree of symmetry and only two degrees of freedom f_1 and f_2. (b) The contour lines of the objective function $\mathcal{F}_{\mathrm{lin}}(\boldsymbol{f})$ are ellipses. In comparison, the contour lines of $\mathcal{F}_{\mathrm{RP}}(\boldsymbol{f})$ are slightly contracted along the axes. The respective optimizers $\boldsymbol{f}^{(\mathrm{RP})}$ and $\boldsymbol{f}^{(\mathrm{lin})}$ of the constrained optimization problems (dots) are the points where the contour lines are tangent to the affine subspace defined by $\boldsymbol{Ef} = \boldsymbol{p}$; see Fig. 3. Because of the contraction along the axes, the optimizer $\boldsymbol{f}^{(\mathrm{RP})}$ is further from the coordinate axis. Physically, this corresponds to a more balanced flow and, thus, a smaller maximum line loading.

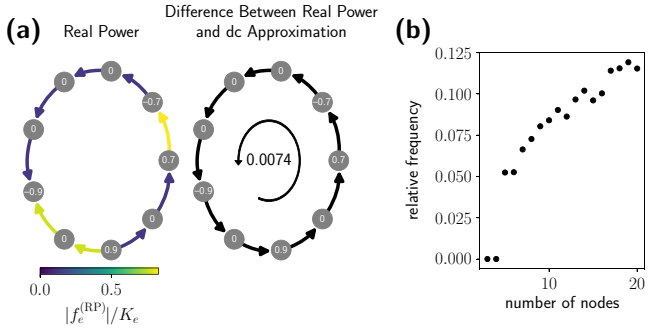

FIG. 6. Maximum line loading of the real power flow and the linear power flow approximation in a cyclic network. (a) An elementary example with $N = 9$ nodes and homogeneous coupling strengths $K_e \equiv 1$ and power injections p_n given in cycles. The left map shows the loading $|f_e^{(\mathrm{RP})}|/K_e$ and the direction of the flow for each edge e. The difference $f_e^{(\mathrm{RP})} - f_e^{(\mathrm{lin})}$ can be expressed as a cycle flow ℓ shown in the right map. Contrary to the geometric intuition developed in Fig. 5, the linear approximation underestimates the maximum line loading $\max_e |f_e|/K_e$. That is, the cycle flow ℓ is parallel to the flow on the most heavily loaded line. (b) For a systematic comparison, we consider networks of different sizes N and 10^6 randomly sampled and valid power injection vectors $\boldsymbol{p}$. For each network we compute the real power flow $\boldsymbol{f}^{(\mathrm{RP})}$ and the linear approximation $\boldsymbol{f}^{(\mathrm{lin})}$. For each N we count the number of networks for which $\max_e |f_e^{(\mathrm{RP})}|$ exceeds $\max_e |f_e^{(\mathrm{lin})}|$ by at least 10^{-4}%. The relative frequency of such networks increases with the size N, reaching approximately 12% for $N = 20$. No such networks are observed for $N \leq 4$.

networks with N nodes and all line parameters set to unity, $K_e \equiv 1$ for all $e \in \mathfrak{E}$. A first example is shown in Fig. 6(a). In this case, we find that the maximum load $\max_e |f_e|/k_e$ is *underestimated* in the linear power flow approximation. This appears surprising but does not contradict our general reasoning. The network includes three very highly loaded edges. The linear power flow overestimates the flow for two of them and underestimates it for only one. Hence, we find that the linear power flow overestimates high loadings *on average*, while we cannot make a general statement for individual lines. We provide a rigorous statement in Lemma 5.

We continue our numerical experiment, considering different network sizes N and use cases. We uniformly sample power injections $\boldsymbol{p}$ such that the grid is balanced $\sum_n p_n = 0$ and compute the real power flow $\boldsymbol{f}^{(\mathrm{RP})}$ as well as the linear approximation $\boldsymbol{f}^{(\mathrm{lin})}$. For each value of N, we count the number of samples where the linear approximation underestimates the maximum loading; that is, $\max_e |f_e^{(\mathrm{RP})}| > \max_e |f_e^{(\mathrm{lin})}|$. Results are shown in Fig. 5(b).

For $N \leq 4$, we find no cases where the linear approximation underestimates the maximum load. The number of cases increases with the cycle length N until it reaches about 12% for a ring with $N = 20$ nodes. Notably, cycles with $N \leq 4$ are special as they do not support multistability [16] and admit explicit stability conditions [1].

D. Properties of real and linear power flows: Rigorous results

We now give two rigorous results on the distribution of line loading and the maximum line loading comparing real and linear power flow. We first show that there are more heavily loaded lines in the linear power flow approximation than in the nonlinear real power flow. To make this statement rigorous, we introduce a function that indicates a heavy loading. Extending Theorem 3, we define the function

$$\hat{\mathcal{G}}_e(f_e) = \mathcal{G}_e(f_e)/\mathcal{G}_e(K_e), \tag{58}$$

which is plotted in Fig. 7. This function increases monotonously and nonlinearly with the line load $|f_e|/K_e$. If a line is weakly loaded, $|f_e| < K_e/2$, then the function is close to zero, $\hat{\mathcal{G}}_e(f_e) < 0.04$. If the function is heavily loaded, $|f_e| \approx K_e$, the function approaches unity. We can

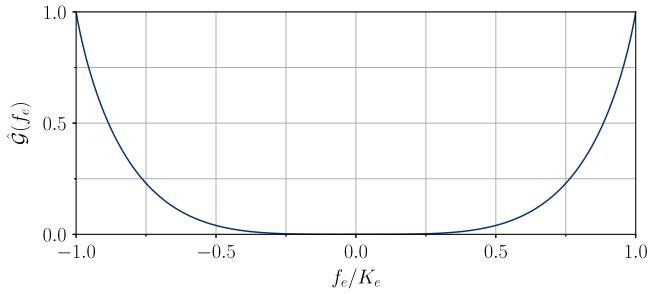

FIG. 7. Dependence of the indicator function $\hat{\mathcal{G}}_e(f_e)$ on the line loading f_e/K_e; see Eq. (58).

thus interpret the function $\hat{\mathcal{G}}_e(f_e)$ as the desired indicator for heavy loading. We can then find the following statement showing that the number of heavily loaded lines is smaller for $\boldsymbol{f}^{(\mathrm{RP})}$ than for $\boldsymbol{f}^{(\mathrm{lin})}$.

Lemma 5. The weighted sum of heavily loaded lines as measured by the indicator function $\hat{\mathcal{G}}_e(f_e)$ satisfies

$$\sum_e K_e \hat{\mathcal{G}}_e(f_e^{(\mathrm{RP})}) \leq \sum_e K_e \hat{\mathcal{G}}_e(f_e^{(\mathrm{lin})}). \tag{59}$$

Proof. We use the notation of Theorem 3. The vector $\boldsymbol{f}^{(\mathrm{RP})}$ minimizes the objective function $\mathcal{F}_{\mathrm{RP}}$. Hence, we obtain

$$\frac{1}{2}\|\boldsymbol{f}^{(\mathrm{RP})}\|_K^2 + \mathcal{G}(\boldsymbol{f}^{(\mathrm{RP})}) \leq \frac{1}{2}\|\boldsymbol{f}^{(\mathrm{lin})}\|_K^2 + \mathcal{G}(\boldsymbol{f}^{(\mathrm{lin})}).$$

Using $\|\boldsymbol{f}^{(\mathrm{RP})}\|_K^2 = \|\boldsymbol{f}^{(\mathrm{lin})}\|_K^2 + \|\boldsymbol{\xi}\|_K^2$, we can rewrite this as

$$\mathcal{G}(\boldsymbol{f}^{(\mathrm{RP})}) \leq \mathcal{G}(\boldsymbol{f}^{(\mathrm{lin})}) - \frac{1}{2}\|\boldsymbol{\xi}\|_K^2 \leq \mathcal{G}(\boldsymbol{f}^{(\mathrm{lin})}).$$

This inequality can be rewritten in components as

$$\sum_e \mathcal{G}(\boldsymbol{f}_e^{(\mathrm{RP})}) \leq \sum_e \mathcal{G}(\boldsymbol{f}_e^{(\mathrm{lin})})$$

$$\Leftrightarrow \quad \sum_e K_e \frac{\mathcal{G}(\boldsymbol{f}_e^{(\mathrm{RP})})}{(\pi-1)K_e/2} \leq \sum_e K_e \frac{\mathcal{G}(\boldsymbol{f}_e^{(\mathrm{lin})})}{(\pi-1)K_e/2}.$$

Using $\mathcal{G}(K_e) = (\pi-1)K_e/2$, we obtain the desired result. ■

As a second step, we consider the two most heavily loaded lines within any cycle of the network. We prove that the ratio of the line loadings $|f_e/K_e|$ is bounded, where the bound is tighter for the real power flow than for the linear power flow. That is, the line loading is more homogeneous.

Lemma 6. Let $\boldsymbol{f}^{(\mathrm{RP})}$ be the solution of the real power flow equations with $\boldsymbol{z} = \boldsymbol{0}$ and let $\boldsymbol{f}^{(\mathrm{lin})}$ be the solution of the linear power flow equations. For every cycle $\mathcal{C}$ in the network, we consider the two most heavily loaded lines a and b, i.e.,

$$\frac{|f_a|}{K_a} \geq \frac{|f_b|}{K_b} \geq \frac{|f_e|}{K_e} \text{ for all } e \in \mathcal{C}\backslash\{a,b\}. \tag{60}$$

Then we have

$$\frac{\arcsin|f_a^{(\mathrm{RP})}/K_a|}{\arcsin|f_b^{(\mathrm{RP})}/K_b|} \leq |\mathcal{C}| - 1,$$

$$\frac{|f_a^{(\mathrm{lin})}/K_a|}{|f_b^{(\mathrm{lin})}/K_b|} \leq |\mathcal{C}| - 1.$$

Proof. We choose a cycle basis such that the cycle $\mathcal{C}$ corresponds to the first fundamental cycle, i.e., the first row of the edge cycle incidence matrix. For the minimizer $\boldsymbol{f}^{(\mathrm{RP})}$, we have

$$0 = \frac{\partial \mathcal{F}_{\boldsymbol{z}=\boldsymbol{0}}}{\partial \ell_1} = \sum_{e\in\mathcal{C}} C_{e1} \arcsin\left(\frac{f_e^{(\mathrm{RP})}}{K_e}\right).$$

Now we can bound the different terms in the sum and obtain

$$\arcsin\left(\frac{|f_a^{(\mathrm{RP})}|}{K_a}\right) = \left|\sum_{e\in\mathcal{C}\backslash\{a\}} C_{e1} \arcsin\left(\frac{f_e^{(\mathrm{RP})}}{K_e}\right)\right|$$

$$\leq (|\mathcal{C}| - 1) \times \arcsin\left(\frac{|f_b^{(\mathrm{RP})}|}{K_b}\right).$$

Replacement of $\mathcal{F}_{\boldsymbol{z}=\boldsymbol{0}}$ by $\mathcal{F}_{\mathrm{lin}}$ yields the corresponding inequality for the linear power flow solution $\boldsymbol{f}^{(\mathrm{lin})}$. ■

This result is particularly useful if we deal with the stationary states of a grid after applying a Kron reduction (see Sec. II). Then the network is fully connected, and we can choose the fundamental cycles to be triangles such that $|\mathcal{C}| - 1 = 2$. We then obtain the following example from Lemma 6. Assume that a line (n,m) is loaded with $f_{nm}^{(\mathrm{RP})}/K_{nm} \geq 99\%$. Then for every vertex $l \neq n,m$, one of the lines (l,m) or (l,n) must be loaded with $f^{(\mathrm{RP})}/K \geq 66\%$. That is, it is impossible for one line to get very heavily loaded in isolation—some lines in the vicinity must be heavily loaded too.

VII. CONCLUSION AND OUTLOOK

The reliable supply of electric power is material for our society. Therefore, it is of central importance to understand which factors determine the operation and stability of the electric power system. In this article, we have analyzed the

stationary states of lossless power grids described by the equations

$$p_n = \sum_m K_{nm} \sin(\theta_n - \theta_m). \tag{61}$$

Because they are nonlinear, there is no straightforward theory of solvability of this set of equations. Furthermore, it has been established that the equations can be multistable depending on the structure of the grid [15,16,20].

In this article, we introduced a novel approach to the stationary states of lossless power grids. The main idea is to shift the attention from the nodes of the grid to the edges and cycles and to reformulate the equations as a convex optimization problem. This formulation provides new insights into the structure of the problem and allows us to derive a series of rigorous results.

The most important results are as follows:

(1) The optimization approach provides a systematic algorithm to systematically compute *all* stationary states that satisfy $|\theta_n - \theta_m| < \pi/2$ for all edges $(n, m) \in \mathfrak{E}$.
(2) The linear power flow or dc approximation is recovered as the quadratic approximation to the optimization problem. This insight allows us to systematically bound the error induced by this approximation.
(3) We have introduced two explicit formulae that provide improved approximations for the real power flows.
(4) The optimization approach provides a geometric interpretation of the network equations. This interpretation provides rigorous results on the existence of solutions.

The computation of all stationary states may still be a computationally hard problem. The optimization formulation facilitates the treatment for a given winding vector $\boldsymbol{z}$, but the number of possible winding vectors may grow exponentially with the size of the network. A detailed analysis of the possible winding vectors $\boldsymbol{z}$ and an upper bound for the number of stationary states is provided in Ref. [20].

The basic idea of this article can be generalized to related network flow problems. First, a generalization beyond the sinusoidal coupling $\sin(\theta_n - \theta_m)$ is straightforward as long as the coupling is antisymmetric and invertible on a certain interval. That is, the set of equations

$$p_n = \sum_m K_{nm} h(\theta_n - \theta_m) \tag{62}$$

with an antisymmetric function h can be reformulated as an optimization problem with the objective function

$$\mathcal{F}(\boldsymbol{f}) = \sum_{e\in\mathfrak{E}} H(f_e/K_e), \tag{63}$$

where H is the primitive of the inverse h^{-1}. Unfortunately, there is no obvious way to include Ohmic losses or coupling function with phase lag in the formalism.

Second, the basic idea may be generalized to the lossless load-flow equations. This set of equations includes the voltage magnitudes and reactive power flows in addition to the real power. Rigorous results on the solvability of the load-flow equations are notoriously difficult to obtain but are of outstanding practical importance.

The data and code that support the findings of this article are openly available [45].

ACKNOWLEDGMENTS

We thank Andrea Benigni, Thiemo Pesch, Manuel Dahmen, and Lukas Kinzkofer for stimulating discussions. The authors gratefully acknowledge support from the Deutsche Forschungsgemeinschaft via Grant No. 491111487.

APPENDIX A: SOLUTIONS OF KCL

In this appendix, we review results on the existence of solutions of KCL with with flow constraints,

$$\boldsymbol{Ef} = \boldsymbol{p}, \quad |f_e| \le K_e \text{ for all } e \in \mathfrak{E}. \tag{A1}$$

In the context of the optimization problems (27) and (32), this is equivalent to the question of whether the feasible set is nonempty. We provide two lemmas to systematically answer this question following Ref. [16].

First, one can map the given problem with multiple sources and sinks to a single-source, single-target flow problem, which is commonly studied in graph theory [46,47]. Given a network with vertex set $\mathfrak{V}$, edge set $\mathfrak{E}$, and edge capacities K_e, we define an extended graph $\mathfrak{G}' = (\mathfrak{V}', \mathfrak{E}')$ by adding two vertices s and t that are connected to the sources and sinks, respectively. That is,

$$\mathfrak{V}' = \mathfrak{V} \cup \{s, t\},$$
$$\mathfrak{E}' = \mathfrak{E} \cup \{(s, n)|p_n > 0\} \cup \{(n, t)|p_n < 0\}.$$

The coupling strengths of the new edges $K_{s,n}$ and $K_{t,n}$ are infinite. Furthermore, we define the cumulative input power and output power:

$$\hat{p}_s = \sum_{n\in\mathfrak{V}, p_n>0} p_n,$$
$$\hat{p}_t = \sum_{n\in\mathfrak{V}, p_n<0} p_n.$$

As usual, we assume that the network is balanced such that $\hat{p}_s = -\hat{p}_t$.

Lemma 7. A solution of KCL with line limits (A1) exists if and only if the maximum $s - t$ flow in the extended network $\mathfrak{G}'$ is larger than or equal to $\hat{p}_s$.

Second, we give a criterion in terms of partitions of the network. Let $(\mathfrak{V}_1, \mathfrak{V}_2)$ be an arbitrary partition of the vertex set $\mathfrak{V}$ such that

$$\mathfrak{V}_1 \cup \mathfrak{V}_2 = \mathfrak{V} \quad \text{and} \quad \mathfrak{V}_1 \cap \mathfrak{V}_2 = \emptyset$$

and let $\mathfrak{E}(\mathfrak{V}_1, \mathfrak{V}_2) = \{(n,m) \in \mathfrak{E} | n \in \mathfrak{V}_1, m \in \mathfrak{V}_2\}$ be the cut set induced by this partition. Define

$$\bar{p}_1 = \sum_{n \in \mathfrak{V}_1} p_n, \quad \bar{p}_2 = \sum_{n \in \mathfrak{V}_2} p_n, \quad \bar{K}_{12} = \sum_{e \in \mathfrak{E}(\mathfrak{V}_1, \mathfrak{V}_2)} K_e.$$

Then we have the following lemma (see Ref. [16] for a proof).

Lemma 8. If for *all* partitions $(\mathfrak{V}_1, \mathfrak{V}_2)$ we have

$$|\bar{p}_1| = |\bar{p}_2| \leq \bar{K}_{12}, \tag{A2}$$

then there exists a solution of KCL with line constraints (A1).

APPENDIX B: NEWTON'S METHOD TO SOLVE OPTIMIZATION PROBLEMS (27) AND (32) FOR ANY WINDING VECTOR z

In Sec. V B we introduced an approximate expression for the solution of the nonlinear real power flow equations. We can iterate this scheme to gradually refine the approximate solution. Hence, we have a tailored algorithm to solve the optimization problems (27) and (32) to obtain $\boldsymbol{f}^{(\mathrm{RP})}$ up to any precision. This algorithm can be formulated for any winding vector $\boldsymbol{z}$, thus providing a method to compute different stable fixed points. The algorithm resembles Newton's method refined to the affine subspace defined by equality constraints; see Chap. 4 in Ref. [48].

We initialize our algorithm by solving the linear problem (39) to obtain $\boldsymbol{f}^{(\mathrm{lin})}$ and set $\boldsymbol{f}^{(0)} = \boldsymbol{f}^{(\mathrm{lin})}$. Then, in each iteration step n, we update our flow vector as

$$\boldsymbol{f}^{(\mathrm{n+1})} = \boldsymbol{f}^{(n)} + \boldsymbol{C}\boldsymbol{\ell}^{(n)}, \tag{B1}$$

where $\boldsymbol{\ell}^{(n)}$ is the solution to the linear system given by

$$\nabla^2 \mathcal{F}_{\boldsymbol{z},\boldsymbol{f}^{(n)}}(\boldsymbol{\ell} = 0) \cdot \boldsymbol{\ell}^{(n)} = -\nabla \mathcal{F}_{\boldsymbol{z},\boldsymbol{f}^{(n)}}(\boldsymbol{\ell} = 0). \tag{B2}$$

Here $\mathcal{F}_{\boldsymbol{z},\boldsymbol{f}^{(n)}}$ denotes the objective function (33) with winding vector $\boldsymbol{z}$ using $\boldsymbol{f}^{(n)}$ as a reference solution of KCL. Furthermore, $\nabla^2 \mathcal{F}_{\boldsymbol{z},\boldsymbol{f}^{(n)}}$ and $\nabla \mathcal{F}_{\boldsymbol{z},\boldsymbol{f}^{(n)}}$ and denote that the gradient and Hessian of this function.

Since $\boldsymbol{C}\boldsymbol{\ell}^{(n)} \in \ker(\boldsymbol{E})$, the linear equality constraints of (27) and (32) are always satisfied if the initial guess $\boldsymbol{f}^{(0)}$ is feasible. Hence, in each iteration, we must check only whether the inequality constraints—that is, the line limits—are not violated. If the line limits are violated in any iteration step, no feasible solution exists, since the feasible space is convex. Computer code to solve optimization problems (27) and (32) using Newton's method can be found in Ref. [45].

APPENDIX C: ADDITIONAL MATERIAL FOR THE PROOF OF THEOREM 3

In this appendix, we provide a technical result used in the proof of Theorem 3. We use the formulation (33) of the objective function with $\boldsymbol{z} = \boldsymbol{0}, \boldsymbol{f}^{(0)} = \boldsymbol{f}^{(\mathrm{RP})}$, and write $\boldsymbol{\xi} = -\boldsymbol{C}\boldsymbol{\ell}$. Then

$$\mathcal{F}_{\mathrm{RP}}(\boldsymbol{f}^{(\mathrm{lin})}) = \mathcal{F}_{\boldsymbol{z}=\boldsymbol{0}}(-\boldsymbol{\ell}),$$
$$\mathcal{F}_{\mathrm{RP}}(\boldsymbol{f}^{(\mathrm{RP})}) = \mathcal{F}_{\boldsymbol{z}=\boldsymbol{0}}(\boldsymbol{0}).$$

Now we apply the multivariate Taylor theorem with the Lagrange form of the remainder, which yields

$$\mathcal{F}_{\boldsymbol{z}=\boldsymbol{0}}(-\boldsymbol{\ell}) = \mathcal{F}_{\boldsymbol{z}=\boldsymbol{0}}(\boldsymbol{0}) - \nabla \mathcal{F}_{\boldsymbol{z}=\boldsymbol{0}}(\boldsymbol{0}) \cdot \boldsymbol{\ell} + \frac{1}{2} \boldsymbol{\ell}^\top \nabla^2 \mathcal{F}_{\boldsymbol{z}=\boldsymbol{0}}(\boldsymbol{\lambda}) \boldsymbol{\ell},$$

where $\boldsymbol{\lambda} \in \mathbb{R}^{M-N+1}$ is a vector with entries λ_α between 0 and ℓ_α. The linear term of the Taylor expansion vanishes because we perform expansion around the minimizer. The quadratic term can be bounded from below. Using the Hessian (34), we obtain

$$\begin{aligned}
&\boldsymbol{\ell}^\top \nabla^2 \mathcal{F}_{\boldsymbol{z}=\boldsymbol{0}}(\boldsymbol{\lambda}) \boldsymbol{\ell} \\
&\quad = \boldsymbol{\ell}^\top \boldsymbol{C}^\top \mathrm{diag}\left(\frac{1}{\sqrt{K_e^2 - (f_e^{(0)} + \sum_\varphi C_{e\varphi} \lambda_\varphi)^2}} \right) \boldsymbol{C}\boldsymbol{\ell} \\
&\quad \geq \boldsymbol{\xi}^\top \mathrm{diag}\left(\frac{1}{K_e} \right) \boldsymbol{\xi} = \|\boldsymbol{\xi}\|_K^2.
\end{aligned}$$

Hence, we obtain

$$\mathcal{F}_{\mathrm{RP}}(\boldsymbol{f}^{(\mathrm{lin})}) \geq \mathcal{F}_{\mathrm{RP}}(\boldsymbol{f}^{(\mathrm{RP})}) + \frac{1}{2} \|\boldsymbol{\xi}\|_K^2.$$

APPENDIX D: PROOF OF LEMMA 4

To prove the inequality

$$\|\boldsymbol{f}^{(c)}\|_K^2 \geq \left(f_a^{(c)}\right)^2 \frac{1}{K_a(1 - K_a \Omega_a)}$$

for each cycle flow $\boldsymbol{f}^{(c)}$ and for each edge $a = (n,m) \in \mathfrak{E}$, we proceed in reverse order. That is, we fix the flow on one

edge a and solve the optimization problem

$$\min_{\boldsymbol{g}} \quad \|\boldsymbol{g}\|_K^2$$
$$\text{subject to} \quad \boldsymbol{E}\boldsymbol{g} = 0, \quad g_a = f_a^{(c)}$$

by the methods of Lagrangian multipliers. We define the Lagrangian

$$\mathcal{L}(\boldsymbol{g}) = \|\boldsymbol{g}\|_K^2 - \sum_n \left[\lambda_n \sum_b E_{nb} g_b\right] - \mu(g_a - f_a^{(c)})$$

and find the stationary points

$$g_{(n,m)} = \begin{cases} K_{nm}(\lambda_n - \lambda_m) & \text{if } (n,m) \neq a, \\ K_{nm}(\lambda_n - \lambda_m + \mu) & \text{if } (n,m) = a, \end{cases}$$

and note that $f_{a=(n,m)}^{(c)} = K_{nm}(\lambda_n - \lambda_m + \mu)$. Hence, the optimizer $\boldsymbol{g}^\star$ generally assumes the form of a potential flow except for the edge a. Hence, we can write it as

$$\boldsymbol{g}^\star = \boldsymbol{K}\boldsymbol{E}^\top \boldsymbol{\lambda} + c\boldsymbol{w}_a,$$

where again $\boldsymbol{w}_a$ is the ath standard basis vector. We now have to determine $\boldsymbol{\lambda}$ and c such that the two constraints are satisfied:

(1) Evaluation of the first constraint $\boldsymbol{E}\boldsymbol{g}^\star = 0$ yields

$$\boldsymbol{E}\boldsymbol{K}\boldsymbol{E}^\top \boldsymbol{\lambda} + c\boldsymbol{E}\boldsymbol{w}_a = 0.$$

With the use of $\boldsymbol{E}\boldsymbol{K}\boldsymbol{E}^\top = \boldsymbol{L}$, this set of linear equations is solved by

$$\boldsymbol{\lambda} = -c\boldsymbol{L}^+\boldsymbol{E}\boldsymbol{w}_a.$$

(2) The second constraint $g_a = f_a^{(c)}$ can alternatively be written as $f_a^{(c)} = \boldsymbol{w}_a^\top \boldsymbol{g}^\star$ and we thus have

$$f_a^{(c)} = \boldsymbol{w}_a^\top \left(c\boldsymbol{w}_a + \boldsymbol{K}\boldsymbol{E}^\top(-c\boldsymbol{L}^+\boldsymbol{E}\boldsymbol{w}_a)\right)$$
$$\Leftrightarrow \quad c = f_a^{(c)} \left(1 - \boldsymbol{w}_a^\top \boldsymbol{K}\boldsymbol{E}^\top \boldsymbol{L}^+ \boldsymbol{E}\boldsymbol{w}_a\right)^{-1}.$$

We can now compute

$$\begin{aligned} \|\boldsymbol{g}^\star\|_K^2 &= \boldsymbol{g}^{\star\top}\boldsymbol{K}^{-1}\boldsymbol{g}^\star \\ &= \left(c\boldsymbol{w}_a^\top + \boldsymbol{\lambda}^\top \boldsymbol{E}\boldsymbol{K}\right)\boldsymbol{K}^{-1}\left(\boldsymbol{K}\boldsymbol{E}^\top\boldsymbol{\lambda} + c\boldsymbol{w}_a\right) \\ &= c^2 K_a^{-1} + \boldsymbol{\lambda}^\top \boldsymbol{L}\boldsymbol{\lambda} + 2c\boldsymbol{w}_a^\top \boldsymbol{E}^\top \boldsymbol{\lambda}. \end{aligned}$$

Inserting the expression for $\boldsymbol{\lambda}$, we obtain

$$\begin{aligned} \|\boldsymbol{g}^\star\|_K^2 &= c^2 K_a^{-1} + c^2 \boldsymbol{w}_a^\top \boldsymbol{E}^\top \underbrace{\boldsymbol{L}^+\boldsymbol{L}\boldsymbol{L}^+}_{=\boldsymbol{L}^+} \boldsymbol{E}\boldsymbol{w}_a \\ &\quad - 2c^2 \boldsymbol{w}_a^\top \boldsymbol{E}^\top \boldsymbol{L}^+ \boldsymbol{E}\boldsymbol{w}_a \\ &= c^2 \left(K_a^{-1} - \boldsymbol{w}_a^\top \boldsymbol{E}^\top \boldsymbol{L}^+ \boldsymbol{E}\boldsymbol{w}_a\right). \end{aligned}$$

Thus, inserting the expression for c and using $\boldsymbol{w}_a^\top \boldsymbol{K} = K_a \boldsymbol{w}_a^\top$, we get

$$\begin{aligned} \|\boldsymbol{g}^\star\|_K^2 &= (f_a^{(c)})^2 \left(1 - \boldsymbol{w}_a^\top \boldsymbol{K}\boldsymbol{E}^\top \boldsymbol{L}^+ \boldsymbol{E}\boldsymbol{w}_a\right)^{-2} \\ &\quad \times \left(K_a^{-1} - \boldsymbol{w}_a^\top \boldsymbol{E}^\top \boldsymbol{L}^+ \boldsymbol{E}\boldsymbol{w}_a\right) \\ &= (f_a^{(c)})^2 K_a^{-1} \left(1 - K_a \underbrace{\boldsymbol{w}_a^\top \boldsymbol{E}^\top \boldsymbol{L}^+ \boldsymbol{E}\boldsymbol{w}_a}_{=\Omega_a}\right)^{-1}, \end{aligned}$$

which concludes the proof by our noting that $\|\boldsymbol{g}^\star\|_K^2 \leq \|\boldsymbol{f}^{(c)}\|_K^2$.

APPENDIX E: MATPOWER 30-BUS TEST CASE

The original MATPOWER 30-bus test case [49] data are intended to be used to study the full ac power flow. Hence, the power injections are balanced only up to losses. In this work, we neglect losses as well as the reactive power flows and thus slightly adapt the MATPOWER 30-bus test case to our needs. We keep the topology and line admittances of the grid but rebalance the real power injections. That is, the real power imbalance $\sum_n p_n$ of the loads and generators is added to the power injection of the first generator to arrive at a balanced grid. To study different grid loads, we introduce a power factor p_f as a multiplicative scalar that rescales the rebalanced power injections, effectively changing the line loading.

[1] F. Dörfler, M. Chertkov, and F. Bullo, Synchronization in complex oscillator networks and smart grids, Proc. Natl. Acad. Sci. **110**, 2005 (2013).

[2] D. Witthaut, F. Hellmann, J. Kurths, S. Kettemann, H. Meyer-Ortmanns, and M. Timme, Collective nonlinear dynamics and self-organization in decentralized power grids, Rev. Mod. Phys. **94**, 015005 (2022).

[3] Union for the Coordination of Transmission of Electricity, Final report on the system disturbance on 4 November 2006, https://eepublicdownloads.entsoe.eu/clean-documents/pre2015/publications/ce/otherreports/Final-Report-20070130.pdf (2007).

[4] Y. Kuramoto, in *International Symposium on Mathematical Problems in Theoretical Physics* (Springer, Berlin, Heidelberg, Germany, 1975), p. 420.

[5] J. A. Acebrón, L. L. Bonilla, C. J. P. Vicente, F. Ritort, and R. Spigler, The Kuramoto model: A simple paradigm for synchronization phenomena, Rev. Mod. Phys. **77**, 137 (2005).

[6] F. A. Rodrigues, T. K. D. Peron, P. Ji, and J. Kurths, The Kuramoto model in complex networks, Phys. Rep. **610**, 1 (2016).

[7] G. Filatrella, A. H. Nielsen, and N. F. Pedersen, Analysis of a power grid using a Kuramoto-like model, Eur. Phys. J. B **61**, 485 (2008).

[8] F. Dörfler and F. Bullo, Synchronization in complex networks of phase oscillators: A survey, Automatica **50**, 1539 (2014).

[9] S. Jafarpour and F. Bullo, Synchronization of Kuramoto oscillators via cutset projections, IEEE Trans. Automat. Contr. **64**, 2830 (2018).

[10] M. Rohden, A. Sorge, M. Timme, and D. Witthaut, Self-organized synchronization in decentralized power grids, Phys. Rev. Lett. **109**, 064101 (2012).

[11] F. Dorfler and F. Bullo, Synchronization and transient stability in power networks and nonuniform Kuramoto oscillators, SIAM J. Control Optim. **50**, 1616 (2012).

[12] P. Varaiya, F. F. Wu, and R.-L. Chen, Direct methods for transient stability analysis of power systems: Recent results, Proc. IEEE **73**, 1703 (1985).

[13] A. E. Motter, S. A. Myers, M. Anghel, and T. Nishikawa, Spontaneous synchrony in power-grid networks, Nat. Phys. **9**, 191 (2013).

[14] D. A. Wiley, S. H. Strogatz, and M. Girvan, The size of the sync basin, Chaos **16**, 015103 (2006).

[15] R. Delabays, T. Coletta, and P. Jacquod, Multistability of phase-locking and topological winding numbers in locally coupled Kuramoto models on single-loop networks, J. Math. Phys. **57**, 032701 (2016).

[16] D. Manik, M. Timme, and D. Witthaut, Cycle flows and multistability in oscillatory networks, Chaos **27**, 083123 (2017).

[17] P. J. Menck, J. Heitzig, J. Kurths, and H. Joachim Schellnhuber, How dead ends undermine power grid stability, Nat. Commun. **5**, 3969 (2014).

[18] R. Delabays, M. Tyloo, and P. Jacquod, The size of the sync basin revisited, Chaos **27**, 103109 (2017).

[19] M. Tyloo, T. Coletta, and P. Jacquod, Robustness of synchrony in complex networks and generalized Kirchhoff indices, Phys. Rev. Lett. **120**, 084101 (2018).

[20] S. Jafarpour, E. Y. Huang, K. D. Smith, and F. Bullo, Flow and elastic networks on the n-torus: Geometry, analysis, and computation, SIAM Rev. **64**, 59 (2022).

[21] J. Machowski, Z. Lubosny, J. W. Bialek, and J. R. Bumby, *Power System Dynamics: Stability and Control* (John Wiley & Sons, Chichester, UK, 2020).

[22] F. Dorfler and F. Bullo, Kron reduction of graphs with applications to electrical networks, IEEE Trans. Circ. Syst. I: Reg. Pap. **60**, 150 (2012).

[23] T. Nishikawa and A. E. Motter, Comparative analysis of existing models for power-grid synchronization, New J. Phys. **17**, 015012 (2015).

[24] F. Hellmann, P. Schultz, P. Jaros, R. Levchenko, T. Kapitaniak, J. Kurths, and Y. Maistrenko, Network-induced multistability through lossy coupling and exotic solitary states, Nat. Commun. **11**, 592 (2020).

[25] P. Arinushkin and T. Vadivasova, Nonlinear damping effects in a simplified power grid model based on coupled Kuramoto-like oscillators with inertia, Chaos Solitons Fract. **152**, 111343 (2021).

[26] C. Balestra, F. Kaiser, D. Manik, and D. Witthaut, Multistability in lossy power grids and oscillator networks, Chaos **29**, 123119 (2019).

[27] R. Delabays, S. Jafarpour, and F. Bullo, Multistability and anomalies in oscillator models of lossy power grids, Nat. Commun. **13**, 5238 (2022).

[28] A. E. Botha, V. Eclerová, Y. M. Shukrinov, and M. Kolahchi, in *15th Chaotic Modeling and Simulation International Conference*, edited by C. H. Skiadas and Y. Dimotikalis (Springer, Cham, 2023), p. 53.

[29] A. R. Bergen and D. J. Hill, A structure preserving model for power system stability analysis, IEEE Trans. Power App. Syst. **PAS-100**, 25 (1981).

[30] H. Sakaguchi and Y. Kuramoto, A soluble active rotater model showing phase transitions via mutual entertainment, Prog. Theor. Phys. **76**, 576 (1986).

[31] S. H. Strogatz, From Kuramoto to Crawford: Exploring the onset of synchronization in populations of coupled oscillators, Physica D **143**, 1 (2000).

[32] R. Delabays, T. Coletta, and P. Jacquod, Multistability of phase-locking in equal-frequency Kuramoto models on planar graphs, J. Math. Phys. **58**, 032703 (2017).

[33] L. Muller, J. Mináč, and T. T. Nguyen, Algebraic approach to the Kuramoto model, Phys. Rev. E **104**, L022201 (2021).

[34] T. Chen and R. Davis, A toric deformation method for solving Kuramoto equations on cycle networks, Nonlinear Dyn. **109**, 2203 (2022).

[35] D. Manik, D. Witthaut, B. Schäfer, M. Matthiae, A. Sorge, M. Rohden, E. Katifori, and M. Timme, Supply networks: Instabilities without overload, Eur. Phys. J. Spec. Top. **223**, 2527 (2014).

[36] K. Purchala, L. Meeus, D. Van Dommelen, and R. Belmans, in *IEEE Power Engineering Society General Meeting, 2005* (IEEE, San Francisco, CA, USA, 2005), p. 454.

[37] B. Stott, J. Jardim, and O. Alsaç, DC power flow revisited, IEEE Trans. Power Syst. **24**, 1290 (2009).

[38] M. E. J. Newman, *Networks—An Introduction* (Oxford University Press, Oxford, 2010).

[39] H. Ronellenfitsch, D. Manik, J. Hörsch, T. Brown, and D. Witthaut, Dual theory of transmission line outages, IEEE Trans. Power Syst. **32**, 4060 (2017).

[40] J. Hörsch, H. Ronellenfitsch, D. Witthaut, and T. Brown, Linear optimal power flow using cycle flows, Electric Power Syst. Res. **158**, 126 (2018).

[41] M. Randić and D. Klein, Resistance distance, J. Math. Chem **12**, 81 (1993).

[42] J. Strake, F. Kaiser, F. Basiri, H. Ronellenfitsch, and D. Witthaut, Non-local impact of link failures in linear flow networks, New J. Phys. **21**, 053009 (2019).

[43] T. Coletta, R. Delabays, I. Adagideli, and P. Jacquod, Topologically protected loop flows in high voltage AC power grids, New J. Phys. **18**, 103042 (2016).

[44] W. Sun and Y.-X. Yuan, *Optimization Theory and Methods: Nonlinear Programming* (Springer Science & Business Media, New York, 2006).

[45] P. C. Böttcher and C. Hartmann, Code accompanying "Synchronized states of power grids and oscillator networks by convex optimization," https://doi.org/10.5281/zenodo.13325174 (2024).

[46] L. R. Ford Jr. and D. R. Fulkerson, *Flows in Networks* (Princeton University Press, Princeton, 2015).

[47] Y. Nussbaum, Multiple-source multiple-sink maximum flow in planar graphs, ArXiv:1012.4767.

[48] S. Boyd and L. Vandenberghe, *Convex Optimization* (Cambridge University Press, Cambridge, UK, 2004).

[49] MATPOWER, 30-bus test case, https://matpower.org/docs/ref/matpower5.0/case30.html (accessed 2023-05-04).